Conservation of Orbital Angular Momentum in Degenerate Four-wave Mixing via Rubidium Vapor

A thesis submitted in partial fulfillment of the requirement
for the degree of Bachelor of Science with Honors in
Physics from the College of William and Mary in Virginia,

by

Kangning Yang

Accepted for Honors

Irina Novikova

Advisor: Prof. Irina Novikova

Keith Griffioen

Prof. Keith Griffioen, Physics

Anya Lunden

Prof. Anya Lunden, Linguistics

Williamsburg, Virginia
May 9 2020

Contents

Acknowledgments

I would like to first thank my advisor Professor Irina Novikova, who not only taught me how to do physics but also how to be a person, penetrating but not biting, easy-going but not conforming. I would also like to thank my lab partner Hana Warner, without whom this experiment cannot be done. I enjoyed every second working with her. Her experimental intuition, creativity, and perseverance is something I always admire and try to catch up. I would like to thank members of Quantum Optics group at W&M who I can always rely on, especially Professor Eugeniy Mikhailov, graduate student Nik Prajapati and Savannah Cuozzo for their tireless advice. Finally I would like to thank my parents and my fiancée Shinong, for always supporting me and making me feel at home even when I am on the other side of the planet.

List of Figures

Abstract

We present an experimental platform which can generate quantum-correlated beams with Orbital Angular Momentum (OAM) via degenerate Four-Wave Mixing (FWM) in Rubidium vapor. We further investigated the conservation of OAM before and after FWM by performing LG mode decomposition using interferometer. To compare our experimental result with theoretical prediction, we simulated a simplified version of our set up. Moreover, we used this toy model to study the conservation of radial and angular intensity profile through changing parameters limited by our set up. In general, we found that FWM preserves most information consisted in OAM, but has a rather loose control over the information stored in radial profile.

Chapter 1

Introduction

In 1992, Allen, Beijersbergen, Spreeuw, and Woerdman published their seminal paper, in which they first introduced the concept of Orbital Angular Momentum (OAM) of light. [1] The discovery that photons, just like macroscopic objects, could carry orbital angular momentum in addition to spin angular momentum led to a deeper understanding of photon. With its unique phase spacial profile, OAM has soon become one of the most interesting transverse optical modes in research. In particular, the Laguerre-Gauss (LG) spatial mode of light, which carries a well-defined OAM of $l\hbar$ per photon has a wide range of applications in both classical and quantum communications. Since LG modes can form an orthogonal set in Hilbert space, in theory there are potentially unlimited number of OAM states. This extra information storage capacity can hugely improve the bandwidth of communications. The performance of communication system based on OAM evolved rapidly, from 8 OAM states in a telescope-to-telescope optical link in 2004 [2] to 200Gbit data rates in free space in 2017 [3].

In order to further push the limit of OAM based communication, we turn to the idea of entangled photon. When two photons are entangled, their quantum states are inseparable regardless of the distance between them[4]. This has the potential to improve the distance limit of OAM transmission. Such entangled photons can be

prepared by phase-matched nonlinear optical processes. Generation of beams with entangle OAM states has been exhibited via sum-frequency generation (SFG), parametric down conversion (PDC), and four-wave mixing (FWM) in semiconductors[5].

In our experiment, we will generate and study the OAM beams via FWM in Rubidium (Rb) vapor. Comparing to solid state process, the advantage of using atomic vapor is that the process is usually more efficient and requires lower light intensity. Thus the first part of the experiment is to quantitatively study the transfer of OAM between beams in a degenerate FWM scheme. The second part of our experiment looks deeper into the propagation of LG spacial modes in FWM, especially around the focus of the beam. So far when studying nonlinear optical processes, most theory makes the assumption that the size of the beams changes slowly inside the nonlinear medium, and thus treat the beams as plane waves. However, in our experiment, LG beams have a more complicated phase profile and cannot be treated as plane waves. In particular, in addition to a phase depending on OAM, there is another phase, known as the Gouy phase, which changes sharply around the focus of the beam. Our goal is to determine how the change in Gouy phase affects the transfer of OAM, and more generally, the propagation of LG modes in nonlinear light-matter interactions.

Chapter 2

Theory

2.1 Four-Wave Mixing

2.1.1 General Description of FWM

FWM is a third order nonlinear optics process which involves 2 input fields and 3 output fields. A schematic representation of non-degenerate FWM is shown in Fig. 2.1. Notice that on the left side there are 2 arrows, but they share the same frequency ω_{pump}. This strong field, also known as the pump, is used twice in the input, indicated by ω_{pump1} and ω_{pump2} respectively. If now we send in another weak field, also known as the probe, with frequency ω_{probe}, then FWM process will cause the generation of a third field, the Stokes field, with frequency ω_s. Meanwhile, probe field is also amplified. If we think from the perspective of photon, then what happened in FWM is very simple. Two photons of ω_{pump} are absorbed by the nonlinear medium, and two photons, one ω_{probe} and the other ω_s are generated. Since the conversion is instantaneous, this means that the two photons must be generated at the exact same time and are correlated. Moreover, this process has to obey the conservation of energy and conservation of momentum. Thus frequency and $\vec{k}$ vector of the Stokes field has to obey the following relationship:

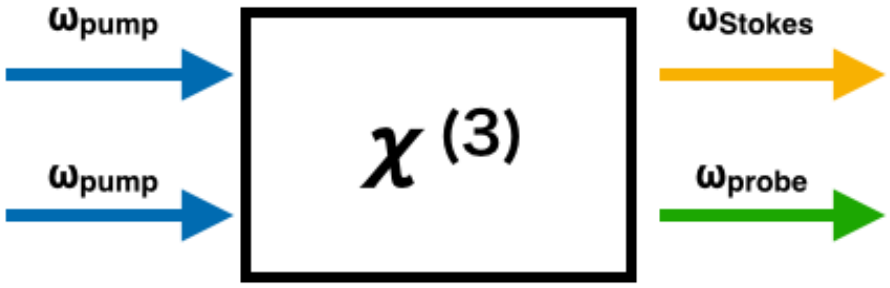

Figure 2.1: Schematic representation of non-degenerate FWM

$$\omega_s = 2\omega_{pump} - \omega_{probe} \tag{2.1a}$$

$$\vec{k}_s = 2\vec{k}_{pump} - \vec{k}_{probe} \tag{2.1b}$$

Fig. 2.2 shows a common set-up of $\vec{k}$ vectors in FWM process. On the left side, pump field comes in along horizontal axis and the Probe field come in the nonlinear medium at an angle. The Stokes field is thus generated after the cell, on the other side of pump field. If we inspect closer and connect the $\vec{k}$ vectors of each field, we would get a closed vector triangle as on the right side of Fig. 2.2.

Figure 2.2: Common line up of fields in FWM. Right side shows the closed triangle of $\vec{k}$ vectors

2.1.2 Classical Description of FWM

In this section we will derive the spacial and temporal behavior of FWM process in atomic vapor. We will start by assuming that our fields are plane waves. We will denote our pump field as ω_c and probe field as ω_p. Thus

$$\vec{E}_c = E_c(r)e^{i(\omega_c t - k_c \cdot \vec{r})}\hat{k}_c \tag{2.2a}$$

$$\vec{E}_p = E_p(r)e^{i(\omega_p t - k_p \cdot \vec{r})}\hat{k}_p \tag{2.2b}$$

$$\vec{E}_s = E_s(r)e^{i(\omega_s t - k_s \cdot \vec{r})}\hat{k}_s \tag{2.2c}$$

Recall that the Maxwell's equations inside homogeneous matter with no free current are:

$$\nabla \cdot \vec{E} = 0 \tag{2.3a}$$

$$\nabla \cdot \vec{B} = 0 \tag{2.3b}$$

$$\nabla \times \vec{E} = -\frac{\partial}{\partial t}(\mu_0 \vec{H}) \tag{2.3c}$$

$$\nabla \times \vec{H} = \frac{\partial}{\partial t}(\varepsilon_0 \vec{E} + \vec{P}) \tag{2.3d}$$

Taking the curl of Eq. 2.3c and substitute the results with Eq. 2.3c, we get the following inhomogeneous wave equation:

$$\nabla^2 \vec{E} - \frac{1}{c^2}\frac{\partial^2 \vec{E}}{\partial t^2} = \mu_0 \frac{\partial^2}{\partial t^2}\vec{P} \tag{2.4}$$

$\vec{P}$ here is the polarization of the medium. It is determined by the properties of the medium and describes how the atoms in the medium interact with incoming fields. Generally, polarization can be expressed in a Taylor series expansion:

$$P_i = \varepsilon_0[\chi_{ij}^{(1)}E_j + \chi_{ijk}^{(2)}E_j E_k + \chi_{ijkl}^{(3)}E_j E_k E_l + ...] \tag{2.5}$$

where P_i is the ith component of the $\vec{P}$. Likewise, E_j is the jth component of the $\vec{E}$ field and $\chi^{(n)}$ is the nth order susceptibility of the medium. Summation over repeated indices are assumed. As we can see from the number of indices for each susceptibility, generally speaking, as nth order susceptibility is a $n+1$ order tensor. Since in a linear medium, only the first term survives, it is also called the linear response. All of the nonlinear optical processes take benefit from the higher order terms. Since medium can have different response to different frequency waves, in most cases susceptibility is frequency dependent.

In the case of atomic vapor, it is possible for us to assume inversion symmetry. Therefore when we invert the sign of the electric fields, the second term in the polarization vector should also be the reverse. Thus we have:

$$\chi^{(2)}_{ijk}(-E_j)(-E_k) = -\chi^{(2)}_{ijk}E_jE_k \tag{2.6}$$

That is, in atomic vapor, the second order susceptibility is always zero. Thus nonlinear polarization vector mainly depends on the third order susceptibility. Moreover, in the case of FWM, we already know the relationship between the frequencies between pump, probe, and Stokes field, described by Eq. 2.1a, the $\vec{P}$ vector for our Stokes field can be written as:

$$\vec{P}^s_i = 3\ \chi^{(3)}_{ijkl}\ E^c_i E^c_j (E^p_k)^*\ e^{i(2\omega_c-\omega_p)t}\ e^{i(2\vec{k}_c-\vec{k}_p)\cdot\vec{r}} \tag{2.7}$$

where $(E^p_k)^*$ is the complex conjugate of the pth component of the probe field. Moreover, after we plug Eq. 2.7 back into Eq. 2.4, we can use it to solve for the spatial behavior of the Stokes field. Here we will use an undepleted pump and probe assumption, presuming that little photon participate in FWM and the intensity of pump and probe does not change in the direction of propagation. Without explicitly showing the full mathematical deduction, we will get the following equation, where c is a constant.

$$\frac{\partial}{\partial r}E_s(r) \ = c\ e^{i(2\vec{k}_c-\vec{k}_p-\vec{k}_s)\cdot\vec{r}} \tag{2.8}$$

Define $2\vec{k}_c - \vec{k}_p - \vec{k}_s$ as Δk, the phase mismatch. Using the initial condition that $E_s(0) = 0$, and the boundary condition that the atomic vapor has a finite length in the direction of Stokes propagation L, then the power of our Stokes field is proportional to the square of a sinc function.

$$P_s(L) \ \propto \ sinc^2(\frac{1}{2}\Delta kL) \tag{2.9}$$

A figure of Eq. 2.9 is shown in Fig 2.3. As we can see from the graph, the power drops really quickly with respect to the length of the medium L. However, under the phase matching condition where $\Delta k = 0$, regardless of L, the sinc function will always equal to 1, the maximum. Therefore FWM has its maximum efficiency under phase matching condition, $\Delta k = 0$, therefore

$$\vec{k}_s = 2\vec{k}_c - \vec{k}_p \tag{2.10}$$

2.1.3 Non-degenerate and Degenerate FWM

Depending on the frequency of pump and probe, FWM can be further divided into 2 subcategories, namely non-degenerate FWM and degenerate FWM. Non-degenerate FWM is usually more often used in experiment via atomic vapor. However, in our experiment, we adopted a degenerate FWM scheme, in which the frequency of the pump and the probe are the same. In this section, I will compare the two types of FWM and discuss why degenerate FWM is especially interesting to us, and how it is different from non-degenerate FWM.

We will begin our discussion of non-degenerate FWM by at how it is achieved experimentally. This part of my discussion is based on the results in R.Ma *et al.*

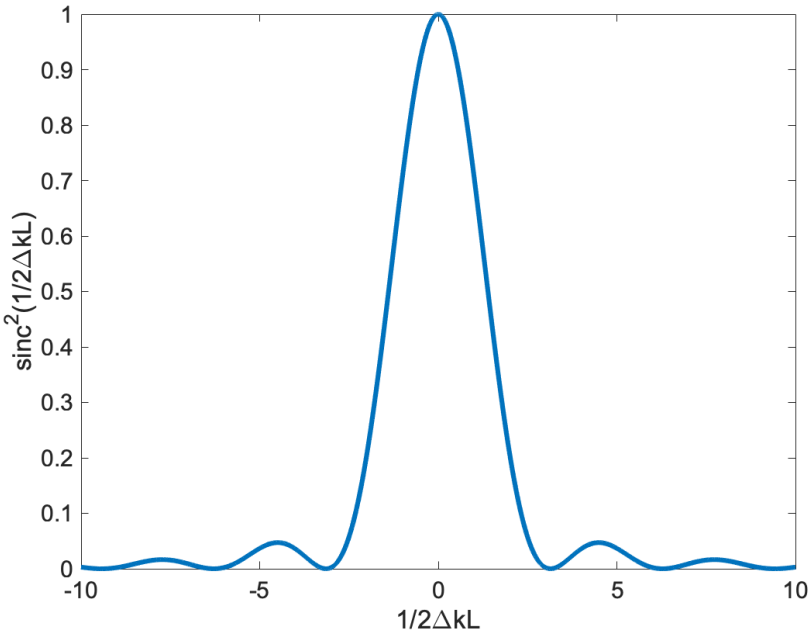

Figure 2.3: sinc function, x-axis is one half of the phase mismatch times the length of the cell. It drops very quickly from the phase-matched position

In their set-up, they use a double-Λ scheme in the D_1 line of ^{133}Cs, as shown in Fig. 2.4. The reason non-degenerate FWM is called this way is because the pump and probe has different frequency. In this configuration, pump (red line) is tuned to the transition between $6S_{1/2}, F = 3$ to $6P_{1/2}, F' = 4$, while probe is tuned to another transition, between $6S_{1/2}, F = 4$ to $6P_{1/2}, F' = 4$. The hyperfine splitting between the two ground levels is $9.2GHz$. However, if we tune the laser exactly to the transition frequency, then we would a huge portion of photon being absorbed by atoms due to the effect of optical pumping. Therefore usually we detune both beam from the transition frequency. Δ is called one-photon detuning, shifting the transition level of one pump photon, while δ is called two-photon detuning because it detunes the transition level of both probe and the other pump photon.

The advantage of non-degenerate FWM is obvious: by detuning from the ab-

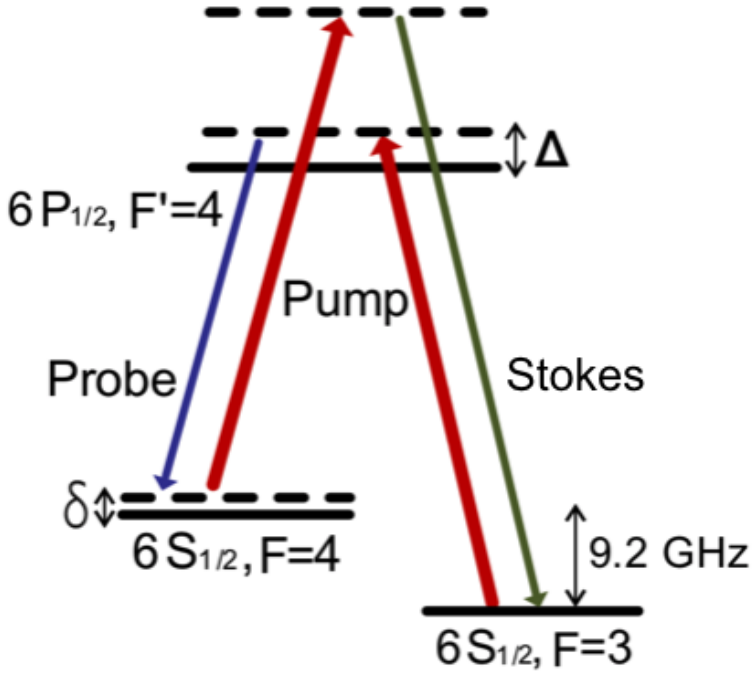

Figure 2.4: Double-Λ non-degenerate FWM scheme of ^{133}Cs used in Ma *et al.*, the hyperfine splitting between the two ground state is 9.2GHz. Δ is one-photon detuning while δ is the two-photon detuning.

sorption line, more photons can possibly participate in FWM process. However the challenge is also demanding. As shown in Eq. 2.2, all the fields in FWM are locked in phase and frequency. Therefore in order to generate high quality correlated fields (narrow bandwidth of beat signal between pump and probe), one must think carefully of how the probe frequency is generated. This often means some methods of phase-locking and frequency-locking. In R.Ma *et al.*, they tried 3 different ways of generating probe: a separate laser source, a phase-locking loop (PLL), and an electro-optic modulator (EOM) which generates side band of the pump laser. Their set-up and the bandwidth of beat signal in each method is shown in Fig. 2.5. Only by using EOM, they were finally able to generate a high quality probe (bandwidth of 1Hz) that can be used in their intensity-squeezing experiment.

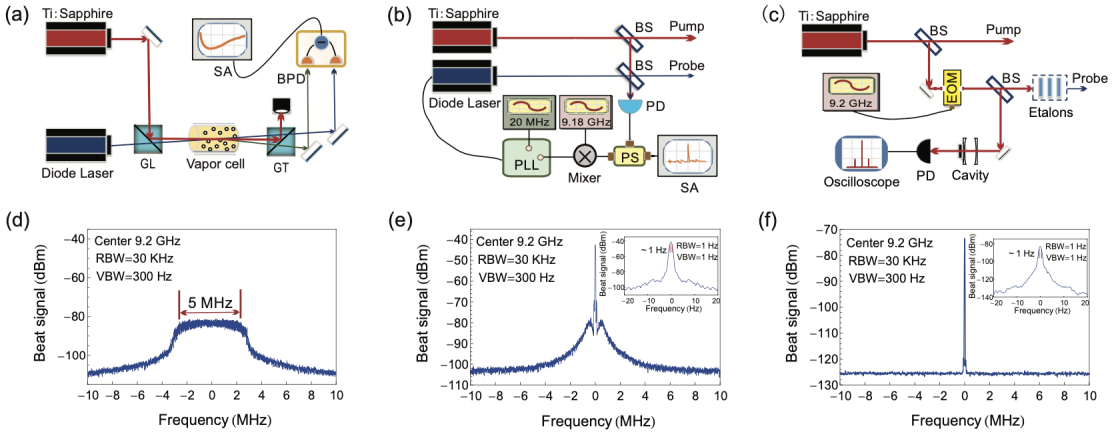

Figure 2.5: Three different experimental setup for the generation of probe in Ma *et al.* and their corresponding beat signal bandwidth. It determines how well the probe is locked with respect to the pump. (a) uses a separate source; (b) uses a PLL; (c) uses EOM. Only probe generated by EOM is well locked in frequency and phase, with a linewidth of 1Hz.

On the other hand, degenerate FWM uses the same frequency for both pump and probe. In our experiment, we use ^{87} Rb atomic vapor as medium, and we lock our laser to the transition $5S_{1/2}, F = 2 \rightarrow 5P_{1/2}, F' = 1$ transition, shown in Fig. 2.6. (Reasons for this choice will be discussed later in experiment and result section.)

Note that in degenerate FWM, the frequencies of all fields are the same. This brings pros and cons. The benefit is that we can use one source for both pump and probe beam, without having to worried about frequency and phase-locking. The drawback is that in order to the phase matching condition in Eq. 2.10, the $\vec{k}$ vector triangle as shown in Fig. 2.2 will be very flat. Thus the angular separation between three beams will be very small. This makes it harder for us to separate the beams and send only Stokes for detection. One solution to this problem is to separate the polarization of the beams. If the polarization of probe and pump beam are orthogonal, there will be less interference, as well as more angular separation between beams, since $\vec{k}$ is generally a function of polarization as well as frequency.

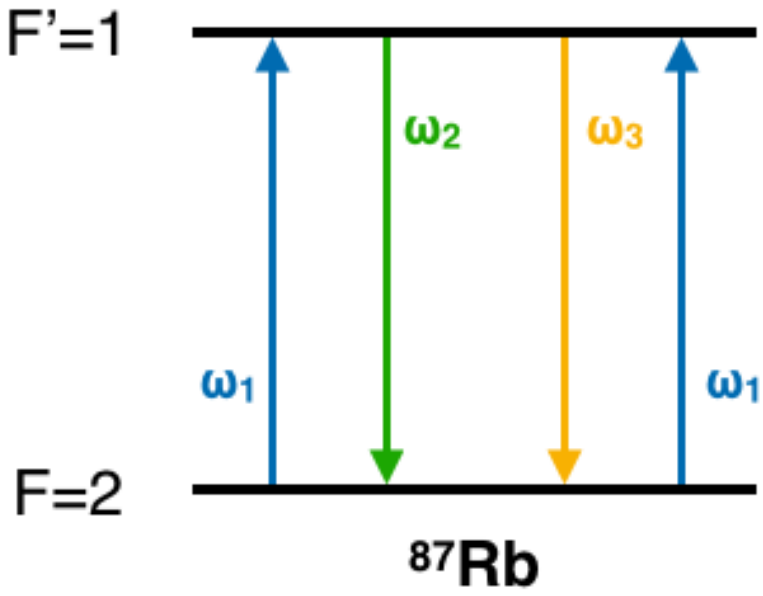

Figure 2.6: Our degenerate FWM level diagram of D1 line in ^{87}Rb, all of the fields are the same frequency. Pump and probe has orthogonal polarization, Stokes polarization is the same as the probe.

Another drawback of degenerate FWM is that while in non-degenerate FWM, one can reduce absorption by detuning, it is impossible to do the same in degenerate FWM, since change in the frequency of laser would result in change in all fields. Therefore we have to find a balance between absorption and FWM process. This requires a fine calibration of the temperature of the Rb cell.

2.2 Orbital Angular Momentum

2.2.1 Brief History of OAM

It is well known that light, a form of electromagnetic wave, can carry linear and angular momentum. In quantum mechanics, we further found out that linear momentum is quantized in the unit of $\hbar$. A photon with $\vec{k_0}$ vector carries a linear momentum of $\hbar\vec{k_0}$. Moreover, in 1936, Beth published his paper, stating that if

the light is circularly polarized, then it can also carry an angular momentum of $\pm\hbar$ depending on the spin of photon. This part of angular momentum is called spin-angular momentum (SAM).

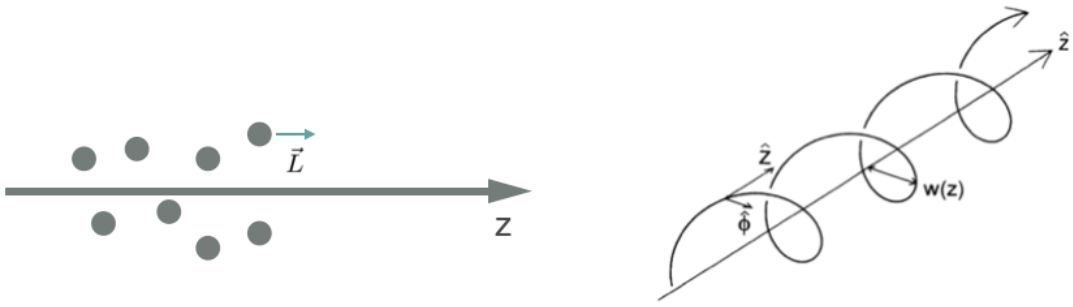

Figure 2.7: Photons carrying OAM traveling in $\hat{z}$ direction. OAM($\vec{L}$) points in the z direction as well. Therefore there must be velocity component in xy plane. Moreover, the Poynting vector should behave like a spiral as shown on the right side.

The origin of OAM, strangely, is easier to understand than that of SAM. As the name suggests, OAM describes the part of angular momentum due to the photon's rotation around its propagation axis. The direction of OAM points in the direction of propagation. Imagine a group of photons traveling in the $\hat{z}$ direction, as shown in Fig. 2.7. In order to have an angular momentum in the $\hat{z}$ direction, it must have linear momentum component in the xy plane. In terms of $\vec{E}$ and $\vec{B}$ field, the angular momentum density $\vec{j}$ can be expressed as

$$\vec{j} = \vec{s} \times (\vec{E} \times \vec{B}) \tag{2.11}$$

In cylindrical coordinate, for $\vec{j}$ to have component in $\hat{z}$ direction, it follows that $\vec{E}$ field or $\vec{B}$ field needs to have component in $\hat{z}$ direction as well. Therefore the Poynting vector of light carrying OAM should behave like a spiraling curve as shown in Fig. 2.7. Since plane waves have Poynting vector pointing straightly towards the direction of propagation, it can never carry OAM. Contrastively, if there is an azimuthal phase

dependence on phase front of the wave, $e^{il\phi}$, and hence the Poynting vector inclined with respect to the beam axis, then light can carry OAM. Fig. 2.8 shows examples of such helical phase fronts, with $l = 1, 2, 3$ and plane wave ($l = 0$).

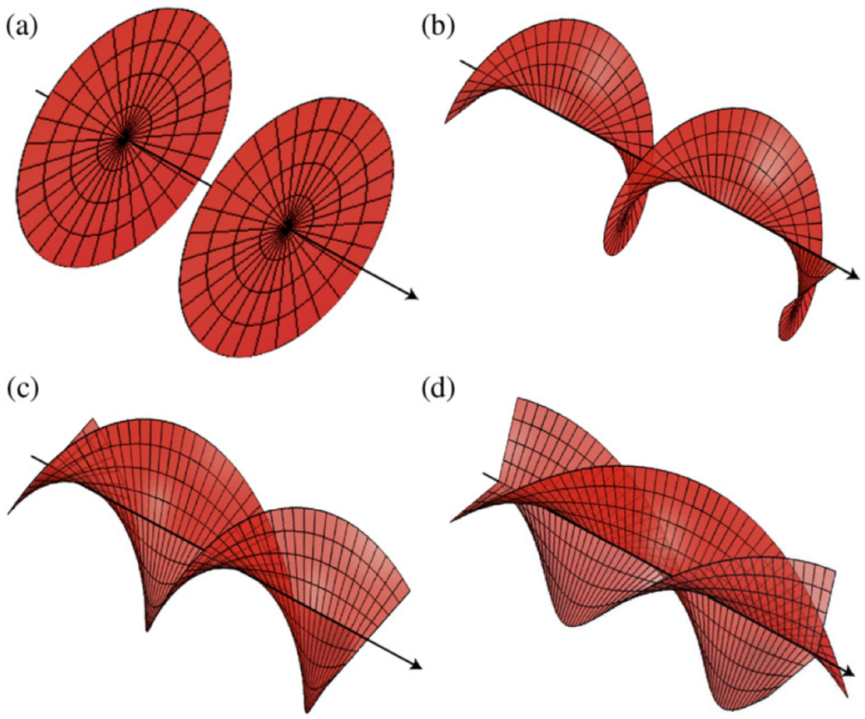

Figure 2.8: Examples of wave with helical wave fronts, the phase of different azimuthal angle is different, shifted by $e^{il\phi}$. (a) is a plane wave ($l = 0$), (b), (c), and (d) has $l = 1, 2, 3$ respectively

In 1992, L.Allen *et al.* published their break through paper, in which they proved that just like linear momentum and SAM of light, optical OAM is also quantized in the unit of $\hbar$, light that has a azimuthal phase dependence $e^{il\phi}$ carries OAM of $l\hbar$. (We will show a simple version of proof in Sec. 2.2.4.) Moreover, they showed that light with Laguerre-Gaussian amplitude profile always have a well-defined OAM. In fact, these profiles form a complete set of orthonormal basis. We refer to them as Laguerre-Gauss (LG) modes. In theory, any beam carrying OAM can be decomposed

into linear combinations of different LG modes.

2.2.2 LG Modes and Phase Singularity

The electric field for LG modes has the following expression

$$LG_p^l(s,\phi,z) = \frac{C_p^l}{w(z)}[\frac{s\sqrt{2}}{w(z)}]^{|l|}L_p^{|l|}(\frac{2s^2}{w^2})e^{-\frac{s^2}{w^2}}e^{ikz}e^{il\phi}e^{\Phi_s+\Phi_G} \tag{2.12}$$

where $C_p^l = \sqrt{2p!/\pi(p+|l|)!}$, $L_p^{|l|}$ is the associated Laguere polynomial. $w(z)$ is the $1/e^2$ beam radius at z. It is a function of z, $w(z) = w_0(1+(z/z_R)^2)^{1/2}$. w_0 is the beam waist and z_R is the Rayleigh range. They are determined by the property of the system. $e^{il\phi}$ is the azimuthal phase dependence that give rise to OAM. There are two more phases which also influence the field, namely the spherical phase front $\Phi_S = ks^2z/(2(z^2+z_R^2))$ and the Gouy phase $\Phi_G = -(2p+|l|+1)arctan(z/z_R)$.

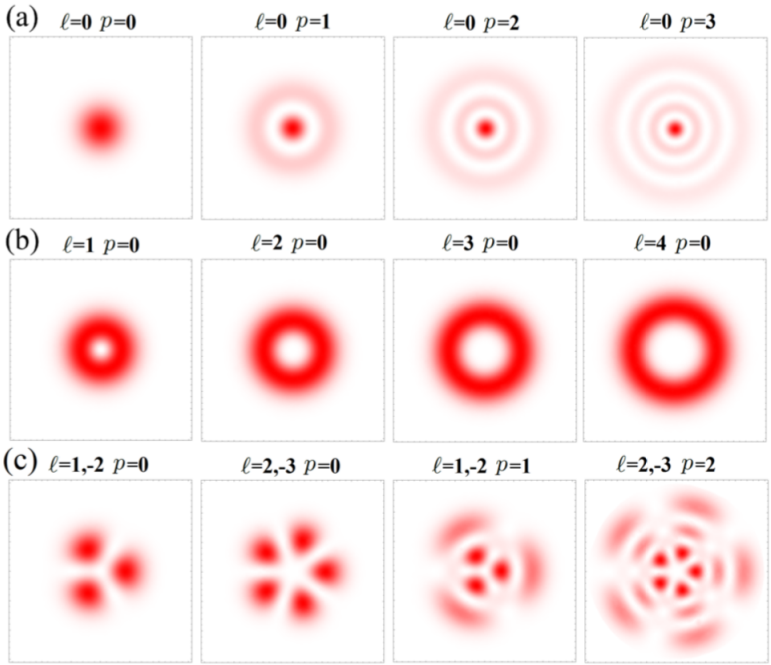

Figure 2.9: Examples of LG modes. FIrst row is different p modes, second row is different l modes, third row is the coherent superpositions of different modes.

The intensity profile for different LG modes is shown in Fig. 2.9. When $l = 0$ (no OAM), LG modes are essentially modified Gaussian beams, with radial ring structures corresponding to the p number. When $p = 1$, there is one ring around the center, when $p = 3$, three rings, etc. Therefore p is also called the radial index. Any paraxial beam with no OAM can be written as a combination of p modes only. On the other hand, when $p = 0$, we can see that the intensity in the center of the beam becomes zero. This is called the phase singularity. The size of phase singularity grows as the l number increases. This is because when we are close to the center of the beam, phase changes rapidly even in a small angle. As a result, all of these phases mashed up together and canceled each other. p mode beams are also referred as doughnut beam because of their shape.

2.2.3 Interference of l modes

Recall that in the last row Fig. 2.9, superposition of multiple LG modes gives us various petal structure. This is due to the interference between LG modes. Since our experiment involves mainly beam of $p = 0$, we will only discuss l modes interference, which corresponds to the first 2 graphs in Fig. 2.9(c).

Imagine two beams carrying different OAM generated from the same source, travel the same path, and are superposed at a certain location z_S along the propagation axis far away from the source. Therefore their beam waist $w(z)$ will be the same, and spherical/ Gouy phase are necessarily zero since $z >> Z_R$. From Eq. 2.12, we know that the two field, $LG_0^{l_1}$ and $LG_0^{l_2}$ at z_S can be expressed as:

$$LG_0^{l_1}(s, \phi, z_S) = D_0^{l_1}(s, z_S) e^{-\frac{s^2}{w^2}} e^{il_1\phi} \tag{2.13a}$$

$$LG_0^{l_2}(s, \phi, z_S) = D_0^{l_2}(s, z_S) e^{-\frac{s^2}{w^2}} e^{il_2\phi} \tag{2.13b}$$

where $D_0^l(s, z_S)$ is some constant determined by s and z_S. When we superpose

these two waves, we will get the result total field at azimuthal angle ϕ will be proportional to the interference term:

$$E_{total}(\phi) \propto \cos(\frac{|l_1| + |l_2|}{2}\phi) \tag{2.14}$$

The intensity of the total field will depend on the azimuthal angle θ. And destructive interference happen in between 0 and 2π. The number of destructive interference angle is decided by the sum of OAM of two beams. One can easily prove that for two beams with l_1 and l_2 respectively, there will be $|l_1| + |l_2|$ destructive angle. Thus the interference pattern will be divided in to $|l_1| + |l_2|$ petals, as shown in Fig. 2.9

2.2.4 Generation of Helical Wave Front Beams

In this section I will discuss two methods that we used to generate beams with helical wave fronts. However, my partner Hana Warner will provide a more detailed description of SLM and how it is programmed. Please refer to her thesis on that part.

Vortex mask

We first tried to use a vortex mask to generate beams with helical wave front. Fig. 2.10 shows a simple sketch of vortex mask. Basically it is an optical element with helical surface. The thickness of the mask increases with the azimuthal angle. It is designed such that when we look at the thickness of this mask from 0 to 2π, then the difference in thickness $s = l\lambda/(n-1)$ where λ is the wavelength of incident light, and n is the refractive index of the mask.

If a light with linear momentum $p = \hbar k_0 = \hbar 2\pi/\lambda$ incident perpendicularly to the flat side of vortex mask at radius r as shown in Fig. 2.10, then according to Snell's law, it will be refracted at an angle θ with respect to perpendicular direction.

$$\sin\alpha \cdot n = \sin(\theta + \alpha) \cdot 1 \tag{2.15}$$

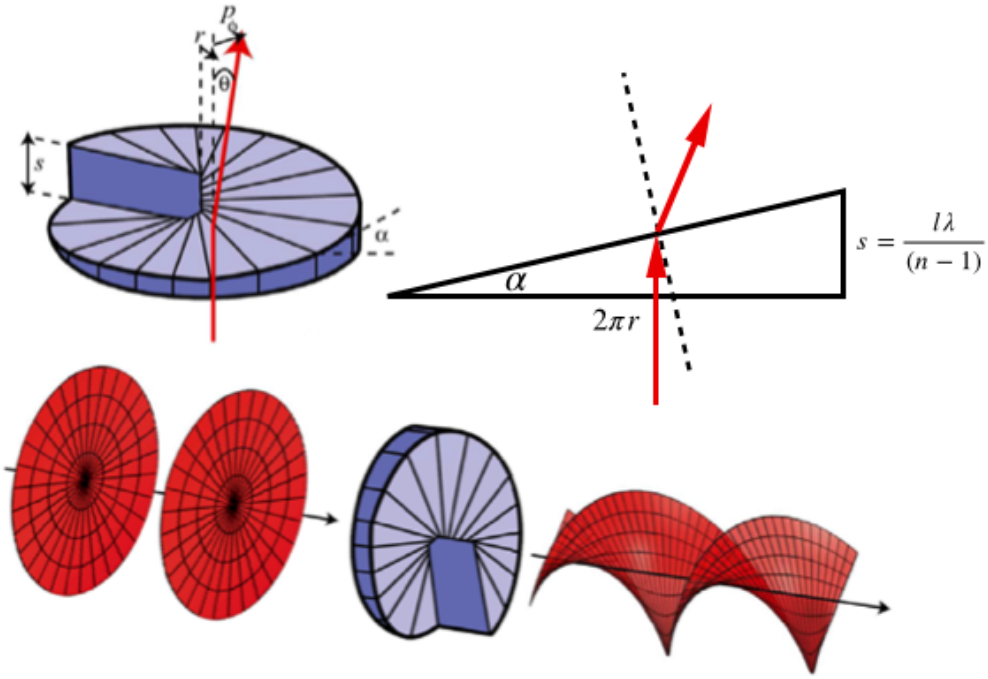

Figure 2.10: Structure of vortex mask. The thickness varies by azimuthal angle gradually. It is designed for particular wavelength and particular l mode. Passing a plane wave to the vortex mask will give a wave carrying OAM of $l\hbar$ per photon.

in which the incident angle α at radius r is

$$\tan\alpha = \frac{s}{2\pi r} = \frac{l\lambda}{2\pi r(n-1)} \tag{2.16}$$

Assume that both α and θ are small angles, we will get

$$\sin\theta = \theta = \frac{l\lambda}{2\pi r} \tag{2.17}$$

On the other hand, the OAM of the photon can be expressed as

$$\vec{L} = \vec{r} \times \vec{p} = rp\sin\theta \tag{2.18}$$

substitute $\sin\theta$ into Eq. 2.19, we can get

$$\vec{L} = rp\sin\theta = r\hbar\frac{2\pi}{\lambda}\frac{l\lambda}{2\pi r} = l\hbar \tag{2.19}$$

Therefore after passing a vortex mask designed for l mode, a photon will carry an OAM of $l\hbar$.

2.2.5 Conservation of OAM in FWM

When we mix pump and/or probe with OAM in FWM process, we can predict the possibility of getting a certain LG modes of Stokes field. Since LG modes forms a complete orthonormal base, we can decompose the input field into linear combination of LG modes. However, we should pay attention here that since Stokes and the amplified probe are generated simultaneously, when we determine a LG mode for Stoke, we are also determining the LG mode for probe, since OAM has to be conserved during the FWM process. Therefore we should denote the coefficient of getting Stokes with l_s and p_s as the following:

$$c_{p_s,p_p}^{l_s,l_p} = \int_{-L/2}^{L/2}\int_0^R\int_0^{2\pi} (LG_{p_c}^{l_c})^*(LG_{p_c}^{l_c})^* LG_{p_s}^{l_s} LG_{p_p}^{l_p}\ s\ d\phi\ ds\ dz \tag{2.20}$$

If we take out ϕ terms and do the integral

$$c_{p_s,p_p}^{l_s,l_p} \propto \int_0^{2\pi} e^{-i(2l_c-l_s-l_p)\phi}\ d\phi \tag{2.21}$$

Therefore the coefficient equals to zero when $2l_c - l_p - l_s \neq 0$. In other case, FWM only generate modes in which OAM is conserved.

$$l_s = 2l_c - l_p \tag{2.22}$$

Chapter 3

Experimental Arrangement

The experimental setup is shown in Fig. 3.1. Before diving into the characteristic of each component. I want to first give an overall description of the system. The whole setup can be divided into two sections: the beam preparation section before the cell and the Stokes analysis section after the cell. While I mainly worked on aligning the Stokes analysis section, my partner Hana worked mainly on the Beam preparation section.

3.1 Beam preparation section

In the beam preparation section, we send our laser signal through fiber and let it pass a polarized beam splitter (PBS), where it is then split into two parts: the strong pump reflects off the PBS, while the weak probe passes through PBS and hits SLM. The phase profile of probe is modified upon hitting SLM and it starts to carry OAM.

It is worth noticing that in our experiment, only probe carries OAM, while pump is always simply a Gaussian beam with no OAM. Since one goal of our experiment is to study the effect of focus (and Gouy phase) on the efficiency of FWM, the two beams may also pass through some lens to add effect of focusing before they enter the Rb cell. The setup shown in Fig. 3.1 is used in one part of our experiment (in

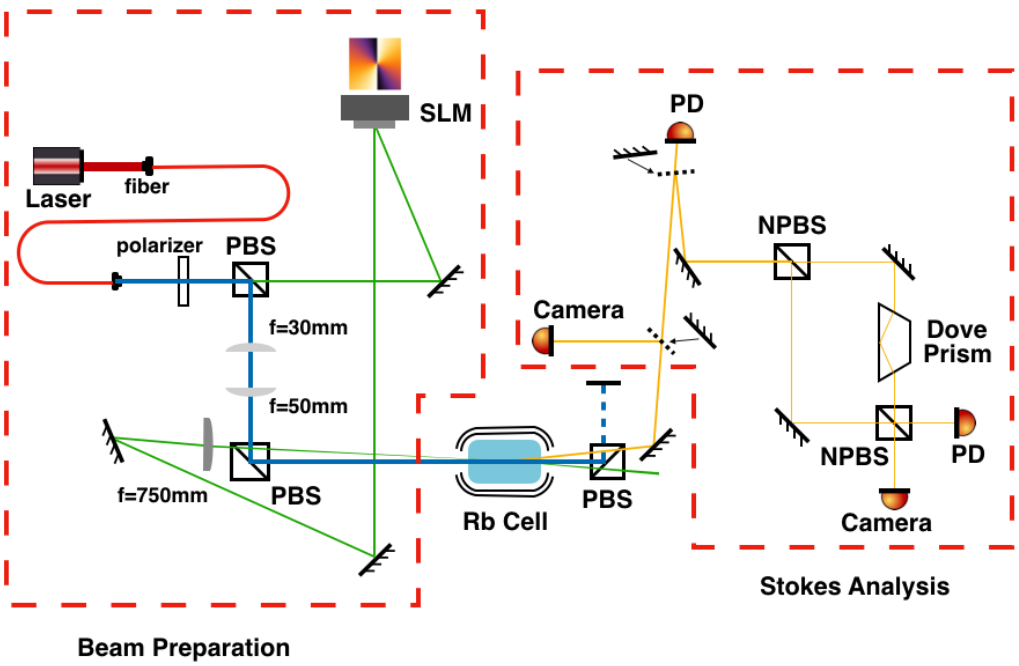

Figure 3.1: The setup of our experiment. It is mainly divided into two sections: beam preparation and Stokes analysis. Beams are color coded, with blue for pump, green for probe, and yellow for Stokes.

Sec. 5.2) where we used a telescope to blow up the size of the pump, as well as a $f = 750$mm lens to slowly focus the probe. The focus condition of our pump and probe for each step of our experiment will be noticed later when we discuss the result.

3.2 Stokes analysis section

After the cell, if the FWM gain is good enough, the Stokes field will be generated. In order to analyze the Stokes, our job is to first get rid of signal from pump and probe. We use another PBS (later polarizer) to block most of the pump signal. As for the probe, since it is further away from the Stokes, we mostly uses an edge mirror or pin hole to physically block its signal.

There are three ways to analyze the Stokes signal. First, and the most straight-

forward way is to observe it on a CCD camera. In this case, usually there is a weak pump leakage in the middle. On its sides, we will find Stokes and probe signal. An example of camera image before and after cell is shown in Fig. 3.2. Camera can give us a rough estimation on the intensity and size of the beams we have, however it can not provide us with precise measurement. Thus our second way of analysis is to use a photodetector and record the power of Stokes field in the sweep range of laser.

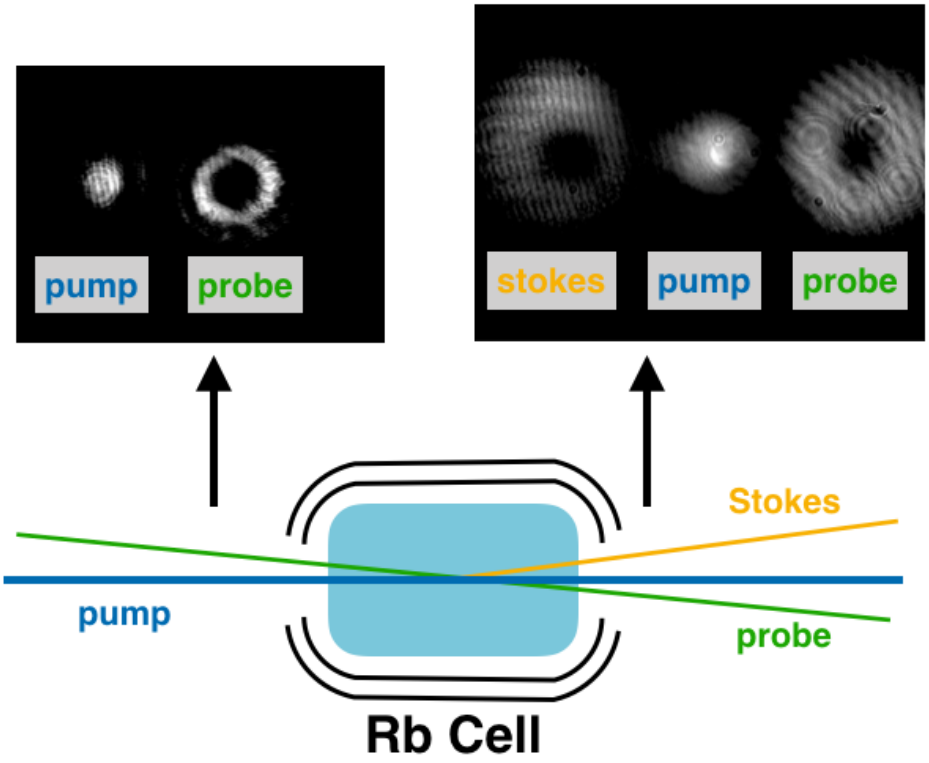

Figure 3.2: Example images we observed on CCD camera before and after cell. Probe carries OAM of $2\hbar$ per photon. The generated Stokes also have phase intensity, meaning that it carries OAM. However, it is not symmetrical, meaning that there are multiple l modes in superposition. Proportion of each mode needs to be send to interferometer for further analysis.

Power measurement is critical because it tells us the efficiency of FWM in our system. However, it can not tell us what LG modes Stokes are generated in, and

what proportion each mode is. For the mode analysis, we rely on the mode analyzer, which is a Zach-Zehnder interferometer with a Dove prism in one arm. The detail of the analyzer will be described in detail in Sec. 5.1

3.3 Rubidium Cell

During the process of experiment, we have tried several different Rb cells. Each has their own merit and limit. Here is a very brief description of their properties and the experiments we did on them.

3.3.1 25mm natural abundance ($30\%^{87}\mathbf{Rb} + 70\%^{85}\mathbf{Rb}$) cell

We used this cell at the beginning of our experiment to check which transition has the best FWM efficiency. We sweep our laser and try to observe at what frequency we found Stokes signal. We switched to the 25mm ^{87}Rb cell after we found only $F = 2 \rightarrow F' = 1$ or 2 transition in ^{87}Rb gives us strong FWM signal. The detail procedures and finding of this experiment can be found in Sec. 4.1.

3.3.2 25mm ^{87}Rb cell

We used this cell to replace the natural abundance cell. The advantage of this cell is that it is short, and thus relatively small absorption effect. On the other hand, short cell also means that there is less distance for overlap between the beams, and thus less FWM gain.

We did several parts of experiment using this cell. First is Stokes optimization, including laser frequency, field polarization, and cell temperature. Data and results for this part is discussed in Chap. 4.

Another attempt we tried in this cell is the preliminary focusing test to observe the effect of Gouy phase. We placed a $f = 75$mm lens in front of the cell such that

its focus is at the center of the cell. We want to see if can still have FWM signal with pump and probe focused, since the focusing in general will give us a wide range of $\vec{k}$ vectors and make it harder to achieve phase-matching condition.

We did not succeed in finding the Stokes. Of course we did several optimization during the process. The description of our procedure and finding will be discussed in Sec. **??**. After all the optimizations we tried, we still was not able to find Stokes signal. Therefore we decided to switch to the 75mm ^{87}Rb + 2.5Torr Ne Cell.

3.3.3 75mm ^{87}Rb + 2.5Torr Ne Cell

The advantage of this cell is that it is long and filled with buffer gas. Buffer gas can decrease absorption, thus letting more photons participate in FWM. Also, since the cell is longer, pump and probe will have more overlap, increasing the chance of FWM. However there is downside as well. Longer cell means that absorption, despite buffer gas, will still be stronger than the previous 25mm cell.

To our disappointment, we were still not able to find Stokes with this new cell. However, when we took out the lens, the Stokes is generated. We decided to use this cell anyway. So we optimized its temperature for this longer cell. This time, we tried to focus only probe with a long focal length lens of $f = 750mm$. We were able to find Stokes this time. We passed our Stokes signal to the M-Z interferometer and performed LG mode decomposition. Results of decomposition can be found in Sec. 5.2.

Chapter 4

Stokes Optimization

The first step in our experiment is to optimize the Stokes signal we can get. There are three parameters that we considered, namely: Laser frequency, polarization of probe, and cell temperature. These optimization are done when pump and probe are both collimated. (No lens in the beam preparation section.) Neither of the beams carry OAM. The pump power is 10.8mW, while the probe power is 2.6mW.

4.1 Laser Frequency

As we have discussed in Sec. 2.1.3, degenerate FWM is very sensitive to laser frequency. However since frequency in all fields are the same, we do not need to detune pump and probe separately. Thus the laser frequency optimization is also rather simple. We just have to sweep our laser and lock our laser at where the FWM gain is the largest.

We used the natural abundance cell described in Sec. 3.3.1 at the beginning of optimization. We mainly looked at the $F = 2 \rightarrow F' = 1$ or 2 transition in ^{87}Rb and $F = 3 \rightarrow F' = 2$ or 3 transition in ^{85}Rb. We recorded the probe spectrum with and without pump, If FWM happens, then there will certainly be less absorption of the probe due to the existence of the pump, since probe will be amplified in FWM. In our case, we observed an obvious decrease of absorption in the transitions described

above.

However, there is no guarantee that Stokes is always generated even when absorption decreased. Because another effect in play is that the pump, with its stronger power, will pump electrons in atom into states inaccessible to probe. (Inaccessible because probe and pump has different polarization, thus have different selection rule in which hyperfine level they can pump electrons onto.) Therefore what we did is to lock at our lasers at each of these transition frequency and look at the signals on camera to check whether if Stokes is generated. Overall, we found that $F = 2 \rightarrow F' = 1$ or 2 transition in ^{87}Rb has a much stronger signal than $F = 3 \rightarrow F' = 2$ or 3 transition in ^{85}Rb. In fact, the power of the later one was to weak that it is hardly detected by CCD. This motivated us to switch the 25mm ^{87}Rb only cell.

After switching the cell, the Stokes signal is much stronger. (Since there was only 30% ^{87}Rb in natural abundance cell). We can now monitor the Stokes power on the photodetector through an oscilloscope, and record the Stokes power and pump leakage during the sweep. An example of the data for laser frequency optimization is shown in Fig. 4.1.

Pay attention that since we record the data from oscilloscope directly, the x-axis on graph is time. However, since we were sweeping our laser, the laser frequency also increase with time. As our Theory has predicted, the frequency of the peak is very close to that of atomic transition. Moreover, from the graph, we see that the first peak, corresponding to $F = 2 \rightarrow F' = 1$ transition has a strong Stokes signal. Therefore we decide to lock our laser at frequency of the first transition.

4.2 Polarization of probe

Next step we optimized the polarization of probe. To do this we inserted a quarter wave ($\lambda/4$) plate before the probe enters the cell. The setup for this part of

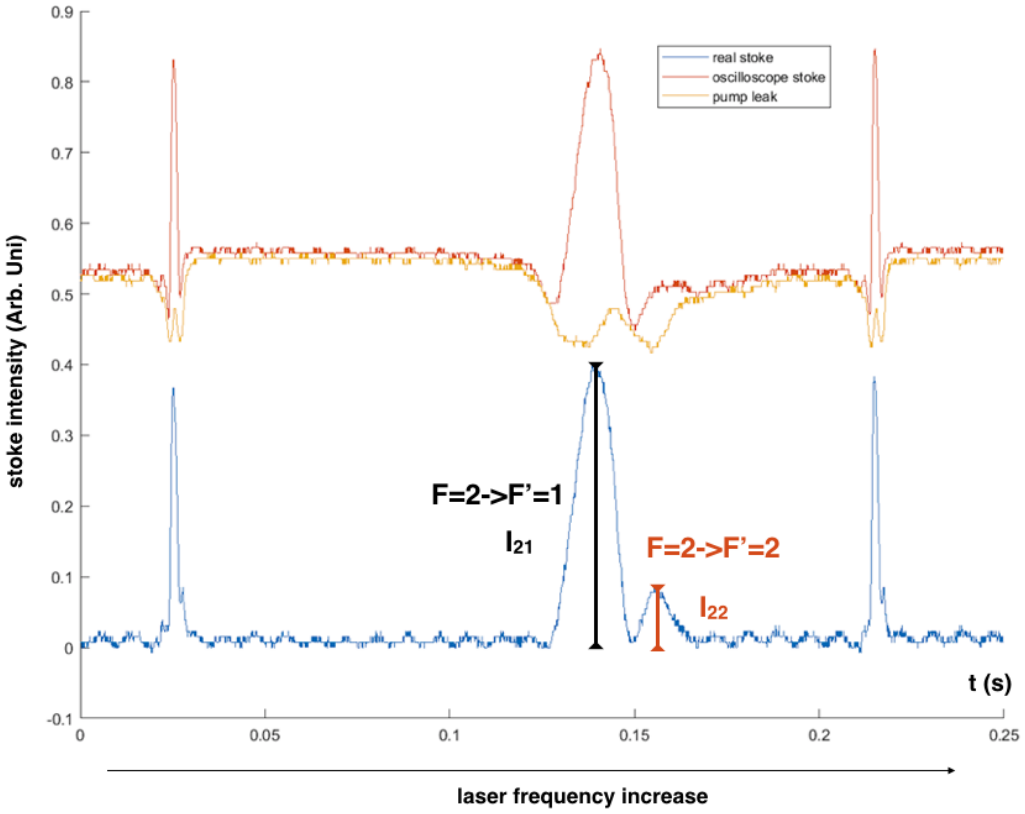

Figure 4.1: Example of Stokes signal on which our laser frequency optimization is based. The red line is the Stokes signal on oscilloscope and the yellow line is the pump leakage which we need to subtract. The blue line is the Stokes power. There are two peaks on the graph, corresponding to $F = 2 \rightarrow F' = 1$ and $F = 2 \rightarrow F' = 2$ transition. We decided to lock our laser on the first transition since Stokes signal is much stronger.

the experiment is shown in Fig. 4.2

The quarter wave plate generally will change the polarization of linearly polarized light into elliptical polarization. When its main axis is parallel to that of linear polarization direction, light will remain linearly polarized. Whereas when it is at 45 degrees to the linear polarization position, it will change the light into circular polarization. In our experiment, we recorded two power measurements. The first is Stokes power in different probe polarization. Second is the probe power after it

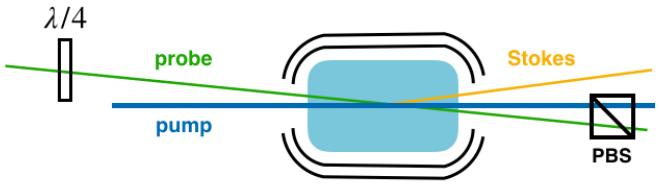

Figure 4.2: Setup for polarization optimization experiment. An additional $\lambda/4$ plate (QWP) is inserted in probe. A PBS is put after the cell.

pass through PBS. This is used as a sign to tell which angle of the QWP is linear polarization. Since only light from the original linear polarization will pass PBS, we would assume any elliptical polarized light has a smaller portion passing through PBS. Therefore the angle when probe power is maximum corresponds to linear polarization.

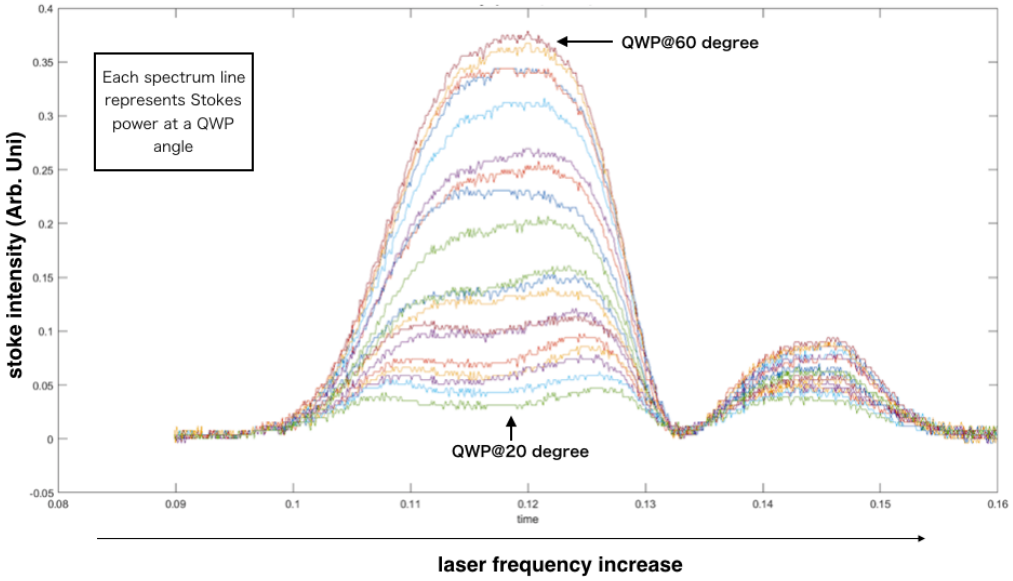

Figure 4.3: Recorded Stokes power spectrum over a range of frequency sweep. Each line represents a different angle of QWP. (0° to 120° in a 10° step)

Fig. 4.3 shows the power of Stokes at different QWP angles. We started from 0° to 120° in a 10° step. After that, we used a Matlab program to select 2 maximum values from each curve, one for each peak. Then we plotted these maximum values

against the QWP angles. We also plotted the probe power as reference. It is shown in Fig. 4.4

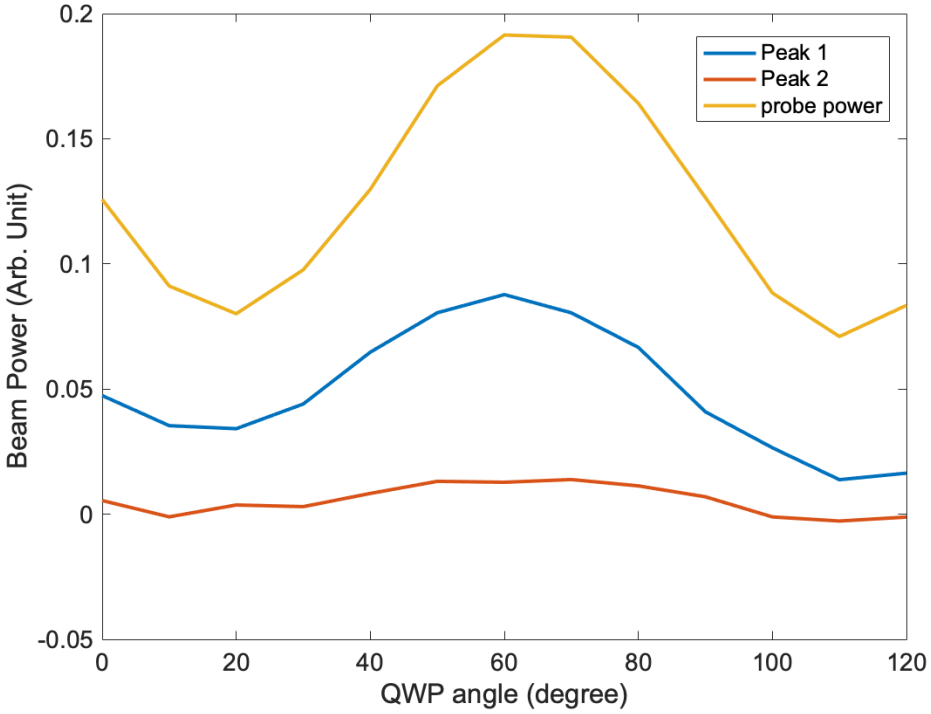

Figure 4.4: Maximum Stokes power in each QWP angle. The blue curve is the maximum value in the first peak, and red curve corresponds to the second peak in Fig. 4.3. Yellow curve is the probe power. We found that Stokes has power maximum when probe is linearly polarized. (maximum probe power at around 60 degree)

From Fig. 4.4 we can see that Stokes power has maximum when probe is linearly polarized, since probe power reaches maximum when light is linearly polarized. (In our case, when QWP is at 60 degree.) Another observation is that regardless of polarization, the maximum of peak 1 ($F = 2 \rightarrow F' = 1$), is always larger than that of peak 2 ($F = 2 \rightarrow F' = 2$). This also confirmed that we should lock our laser at the first transition.

4.3 Cell Temperature

Our last optimization is on the temperature of the cell. Higher temperature will increase the nonlinear susceptibility $\chi^{(3)}$ of our medium, however it would also increase the absorption. Therefore our job is to find an optimal temperature that balance the two effects and provides us with the strongest Stokes signal. The result is plotted in Fig. 4.5. We optimized out cell temperature to $69°C$.

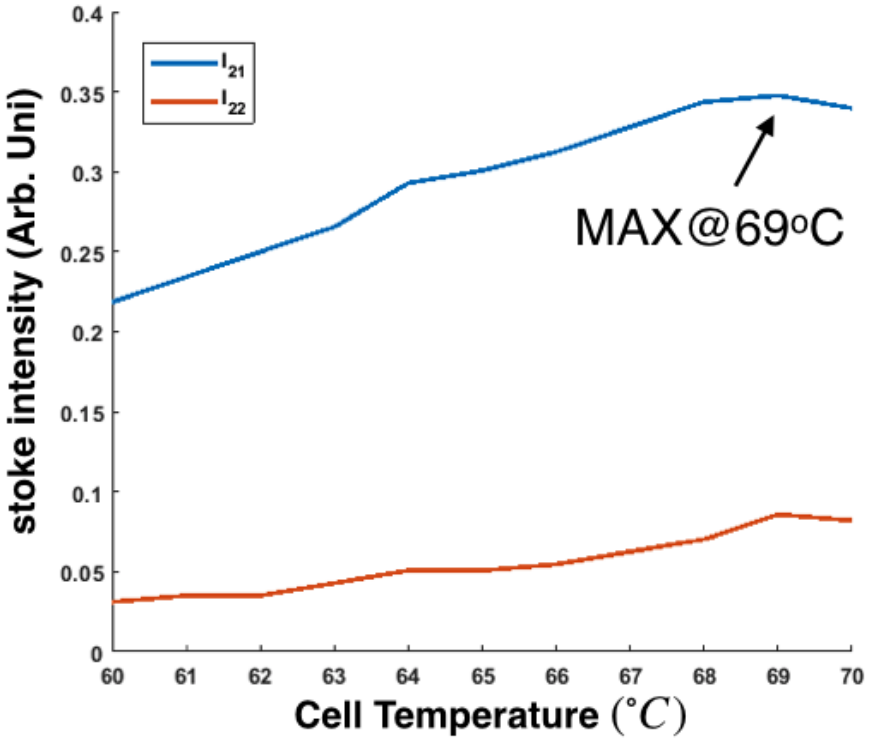

Figure 4.5: Stokes power against cell temperature. At $69°C$, Stokes reaches maximum and then start to decline.

Chapter 5

Petal Analysis

In this section, I will discuss the experiment procedure and results of Stokes mode decomposition when we used the 75mm ^{87}Rb Cell and a $f = 750mm$ long focal length lens in probe. The setup of this part of the experiment is the same as shown in Fig. 3.1. The goal of mode decomposition is to give a qualitative account on what modes are generated in FWM. We profiled both pump and probe beam in our system. The pump is a collimated beam with beam waist $w_{c0} = 2.7$mm, and probe is a slowly focusing beam, with beam waist $w_{p0} = 0.35$mm at cell center, and a Rayleigh range of $z_R = 471mm$. Therefore in this condition $z_R >> L$, the length of our cell. The beam profile around the cell position is shown in Fig. 5.1.

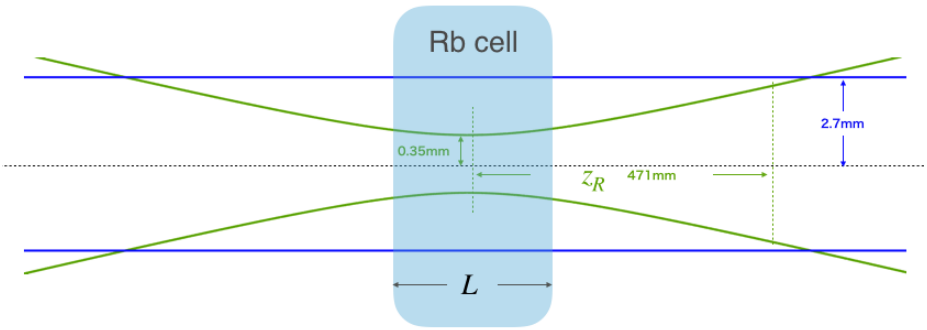

Figure 5.1: Pump and Probe beam profile around the focus position. Probe waist is $w_{p0} = 0.35$. Pump waist is $w_{c0} = 2.7$mm. Probe in Rb cell is much smaller than pump. Also notice that $z_R >> L$.

5.1 Mode Analyzer

Before discussing the result of the petal analysis. I want to first discuss how the mode analyzer works. Recall from our setup Fig. 3.1, The Stokes field is generated after Rb cell and is send to the mode analyzer. It is a Mach-Zehnder interferometer with one Dove prism in one of the two arms. What Dove prism does is it flips the image. For a beam with OAM of $l\hbar$, this means that Dove prism changes its OAM into $-l\hbar$. The structure of Dove Prism is shown in Fig.5.2. Imagine a beam carrying OAM $l\hbar$ injecting into Dove prism. We will pick one photon which is higher than the beam axis, traveling towards right and out of the page due to its OAM. Photons in this beam thus rotates in clockwise direction. As we can see from the figure, after it travels through the prism, it will be lower than the main axis, but still going out of the page. Now the photons will be rotating counter-clockwisely around the axis. Thus OAM also flips sign and change from $l\hbar$ to $-l\hbar$.

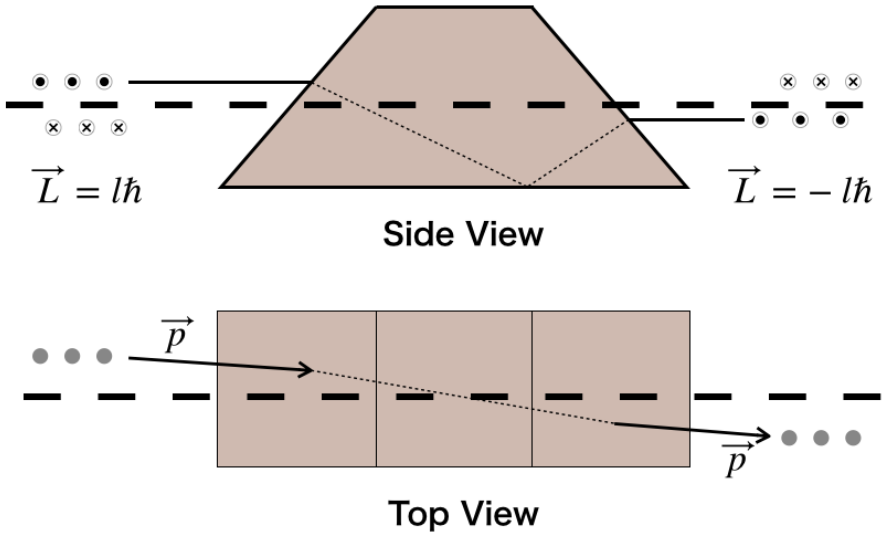

Figure 5.2: Side view and top view of Dove prism. It flips the incoming beam, and outputs mirrored image. For beams carrying $l\hbar$ OAM per photon, Dove prism reverse its sign and make its OAM $-l\hbar$ per photon.

We then send the two beams to interfere on a CCD camera. Recall from Sec. 2.2.3, beams carrying opposite sign of OAM will interfere and gives a petal structure. The number of petals is determined by the sum of absolute value of the two input beams. In out case, one arm is the original Stokes with $l\hbar$, the other is the mirrored Stokes with $-l\hbar$. Therefore the number of petal will always be $2l$. Example of interference pattern and individual arm signal we see on CCD camera is shown in Fig. 5.3. The Stokes has $l = 2$ in the input, and we see four petals in the interferogram, just as we expected. Showing that the dominant mode in this beam is $l = 2$. However we cannot tell just from looking at the image, whether if other modes also present in the Stokes.

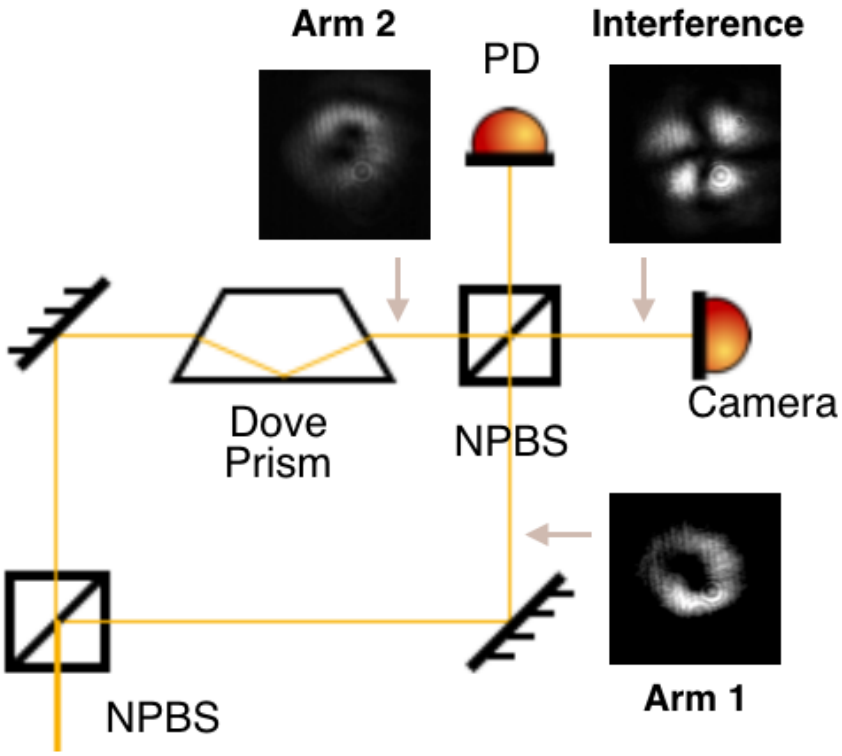

Figure 5.3: Example of interference after the M-Z interferometer. Image of individual arm is shown, as well as the interference pattern when both channel is open. The input Stokes has $l = 2$, and we see $2l = 4$ petals in the interferogram.

In order to inspect what modes are generated in FWM process, we take screen-shots of interferograms and use a Matlab program to further investigate the mode decomposition.

5.2 Mode decomposition program

We record interferograms of Stokes field like that shown in Fig. 5.3. When analyzing the mode, we run into the question of whether the generated Stokes is a coherent superposition of LG modes or a statistical mix of the modes, with no interference between different modes. Here we follows the argument from R.F. Offer [5]. If Stokes is a superposition of modes, then by interference, components inside it can interfere with each other. For example, if Stokes is a superposition of $l = 1$ and $l = 2$ modes, then $l = 1$ modes can interfere with $l = 2$ modes, causing a petal like pattern with constructive and destructive interference before it even enters the interferometer. Since we do not see such interference pattern in our mode, we shall take it as a statistical mixture of different modes.

Then the interferogram is just simply the intensity sum of the interferogram of each l mode. Thus the overall intensity on a certain radius r and angle θ is:

$$I(r,\theta) = \sum_l C_0^l R_0^l(r) \cos^2(l\theta + \phi_0^l) \tag{5.1}$$

where C_0^l is the relative power in a l mode, $R_0^l(r)$ is the spacial profile of this l mode, ϕ_0^l is a phase used to adjust which angle $\theta = 0$ is set at, since $\theta = 0$ on the camera is not necessarily the same θ when Stokes is generated.

In order to fit our data to this model, we need to put our interferogram in a polar coordinate. This is achieved on computer, where we pick a center for the beam. The program then performs a Fourier Transform and illustrates the intensity profile of the beam in this polar coordinate. The program will then compare the intensity profile

of our beam with those of l mode basis and fit the intensity curve by combination of these modes. An example of the intensity profile of our beam is shown in Fig. 5.4

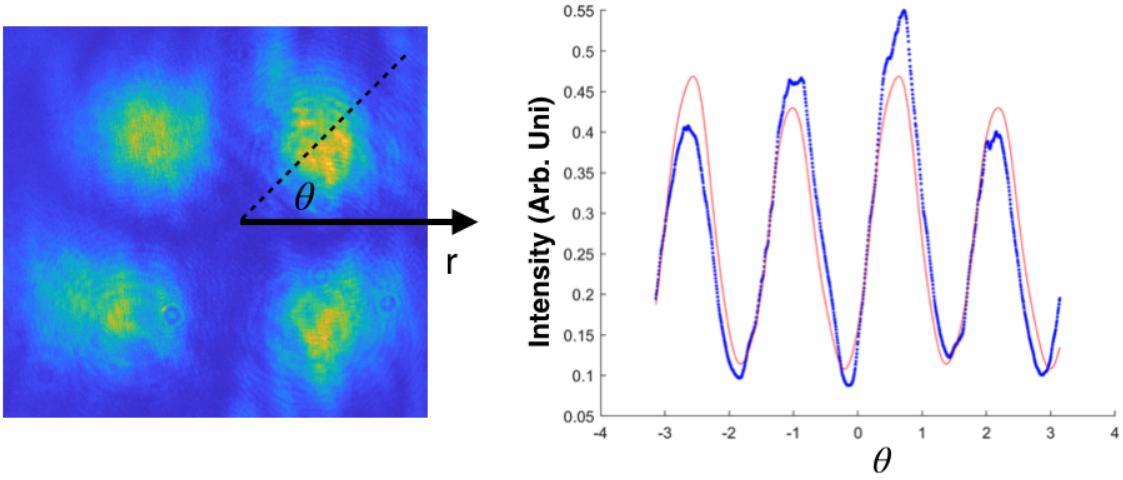

Figure 5.4: Intensity profile of the $l = 2$ Stokes interferogram experimental data. (4 petals because $2l = 4$). The blue curve is our data, and red line is the fit of the program, using intensity profile of pure l modes.

5.3 Results of petal analysis

After running through the fit, the program will tell us what modes are in the Stokes as well as their corresponding relative amplitude in a bar graph. We run analysis of our Stokes when we send from $l = 1$ to $l = 5$ probe beam into the system. Fig. 5.5 shows the original interferogram, and the result of mode decomposition of $l = 2$ probe beam. Fig. 5.6 shows that of the $l = 5$ probe beam.

What is interesting about these results is that while we have a rather pure Stokes signal when l in probe beam is low, the signal becomes more noisy as the input OAM increases. We have two hypothesis on why this might happen. First is that the probe signal, since it is also generated by SLM, can be imperfect in the first place. Second is that this result agrees with the spiral bandwidth broadening reported in R.F. Offer

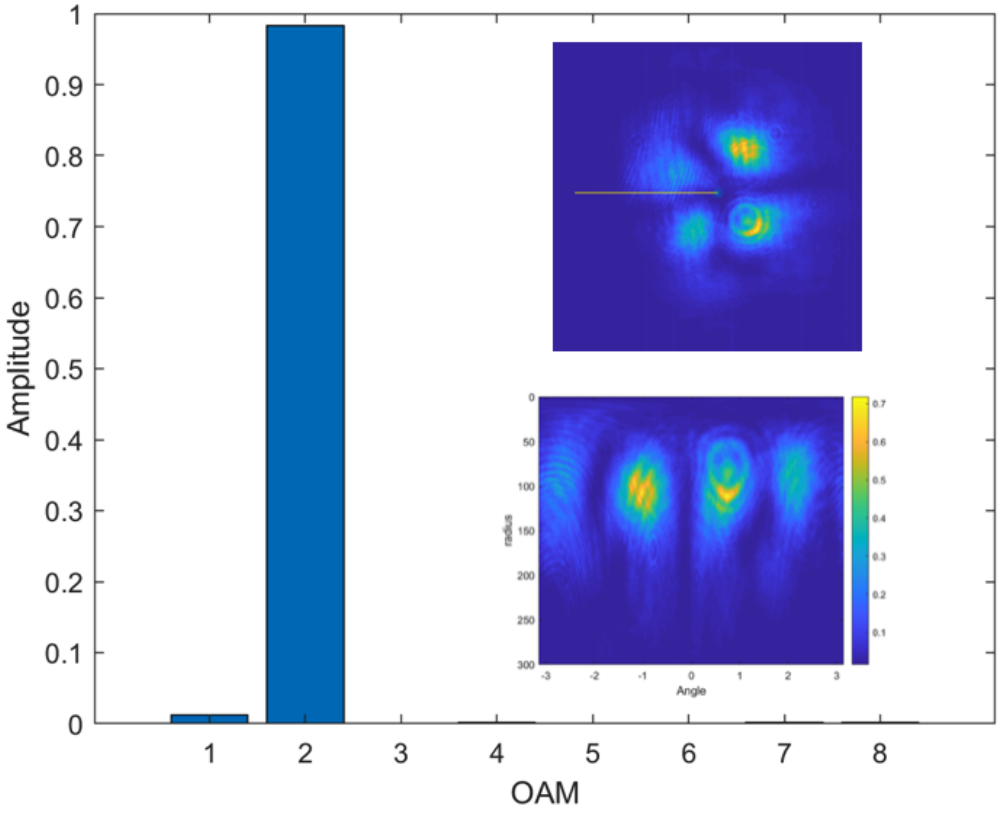

Figure 5.5: The interferogram and mode decomposition result of $l = 2$. We can see from the bar graph that $l = 2$ is the dominant mode, with a small amplitude in $l = 1$ mode.

[5], in which he stated that when $z_R/L >> 1$, the spread of possible OAM of Stokes will be larger compared to when $z_R/L << 1$.

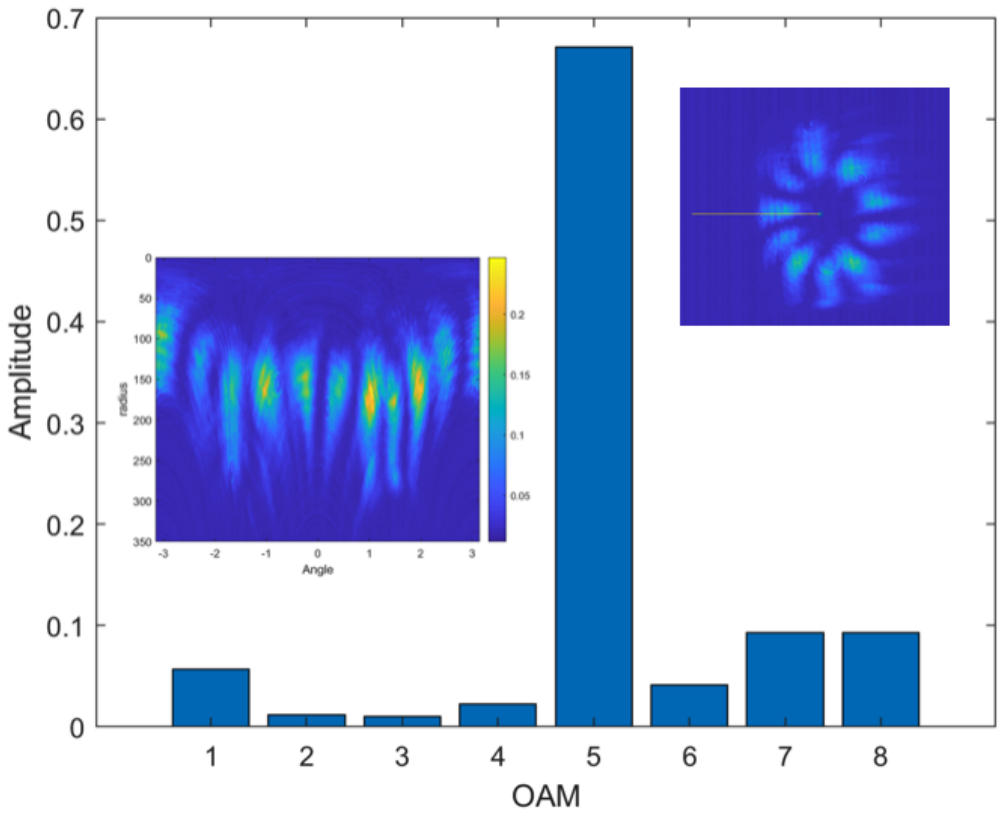

Figure 5.6: The interferogram and mode decomposition result of $l = 5$. Note that although $l = 5$ mode still dominates, other modes has a higher amplitude compared to $l = 2$. Especially higher modes like $l = 7, 8$.

Chapter 6

Computational Simulation

6.1 Motivation

After confirming OAM conservation in our experiment through petal analysis, we can conclude that the l mode information is rather well preserved in degenerate FWM. However, there remain two questions that need answers. First is the efficiency of the l mode transition. Our current setup is set at fixed beam radius: 300 μm for pump and 130μm for probe respectively. It is not necessarily the best option for Stokes generation. We are curious to see whether if shrinking or blowing up the size of the probe beam will increase the FWM gain, thus giving us a higher Stokes power that contains the l mode information.

The second question is whether the information contained in the p mode of LG mode beams will be preserved after FWM. p mode describes the radial intensity information and therefore is very sensitive to the beam radius. Like l mode, we can describe the dominant p mode given the cross-section image of a certain beam. However, this way it is hard to precisely determine the exact component involved in the beam. Moreover, petal analysis cannot extract information about p mode. Thus we need a different method which can perform p mode decomposition.

It is worth noticing that a critical component to answering both questions is the

ability to vary the beam size, which is not very easy to implement in our experiment setup. Therefore in order to gain more freedom in controlling the beam size, we decided to build a FWM model using Mathematica, and run computational simulation to find answers to these two questions. Another advantage of using simulation instead of experiment data is that it largely reduced the difficulty of p mode decomposition as the image we generated will not be influenced by misalignment and possible defects in lens or camera.

6.2 Theoretical Model

In order to model our experimental setup, which is a complex system with three different optical field interacting with atoms inside an atomic vapor cell, we need to make multiple simplifications to our model. In this section we will start from the inhomogeneous wave equation which we introduced in Chapter 2, and simplify it to a set of coupled differential equations that can be solved numerically for FWM process.

For reference, the inhomogeneous equation is restated below again.

$$\nabla^2 \vec{E} - \frac{1}{c^2}\frac{\partial^2 \vec{E}}{\partial t^2} = \mu_0 \frac{\partial^2}{\partial t^2}\vec{P} \tag{6.1}$$

The first approximation which we will make here is to assume that the polarization vector $\vec{P}$ on the righthand side can be expanded through perturbation theory into:

$$P_i = \varepsilon_0[\chi_{ij}^{(1)} E_j + \chi_{ijkl}^{(3)} E_j E_k E_l + ...] \tag{6.2}$$

This is a common simplification in non-degenerate FWM. However, we must make the clarification here since it is not the most precise picture in our degenerate FWM scheme. In our experiment, the transition in Rb atom is resonantly excited such that perturbation theory fails to provide an adequate description, and the power series in Eq. 6.2 does not converge. Linking it back to the physics picture, it is saying that

the refractive index (third-order susceptibility $\chi^{(3)}$) for the probe and Stokes field is different than usual due to the existence of the strong pump field in our experiment. A more precise treatment for degenerate FWM would involve solving density matrix using two-level approximation [6]. However, in our toy model, the absolute correct value of susceptibility is not important. This simplification can be justified as we are only interested in comparing the relative power of the fields, and the susceptibility can be treated as a fixed constant.

$\chi^{(3)}$ is a fourth-rank tensor, and the value of each of its component is dependent on the frequencies of the three input fields. However, since the input frequencies of degenerate FWM are all the same, the expression for polarization vector $\vec{P}$ can be simplified further to one term using the intrinsic permutation symmetry of degenerate FWM and the orthogonal polarization of pump and probe beam.

$$\vec{P}_{Stokes} = 3\chi_{1221}[\vec{E}_{Pump1} \cdot \vec{E}_{Pump2}]\vec{E}^*_{Probe} \tag{6.3}$$

$$\vec{P}_{Probe} = 3\chi_{1221}[\vec{E}_{Pump1} \cdot \vec{E}_{Pump2}]\vec{E}^*_{Stokes} \tag{6.4}$$

Eq. 6.1 can be further simplified if we introduce field $\vec{E}$ propagating along z axis.

$$\vec{E}(\vec{r}, t) = \mathcal{E}(\vec{r}_\perp, z)e^{ikz}e^{-i\omega t} \tag{6.5}$$

where $\mathcal{E}$ denotes the information contained in the perpendicular spacial profile of the beam. It can generally depend on coordinates orthogonal to direction of propagation $\vec{r}_\perp$ (x, y), and z. If we substitute Eq. 6.5 along with the paraxial approximation ($|k\partial\mathcal{E}/\partial z| >> |\partial^2\mathcal{E}/\partial z^2|$), Eq. 6.1 will be simplified into

$$(\frac{\partial}{\partial z} - \frac{i}{2k}\nabla^2_\perp)\mathcal{E} = \frac{ik}{2\epsilon_0}\mathcal{P} \tag{6.6}$$

The second term on the left hand is a Laplacian term which depends on the perpendicular profile of the beam. When the input wave is a plane wave, meaning that $\mathcal{E}(r_\perp, z) = A\mathcal{E}(z)$ has a uniform perpendicular spacial profile, this term becomes zero, and therefore Eq. 6.6 can be solved analytically. A schematic description for this situation is shown in Fig. 6.1(a).

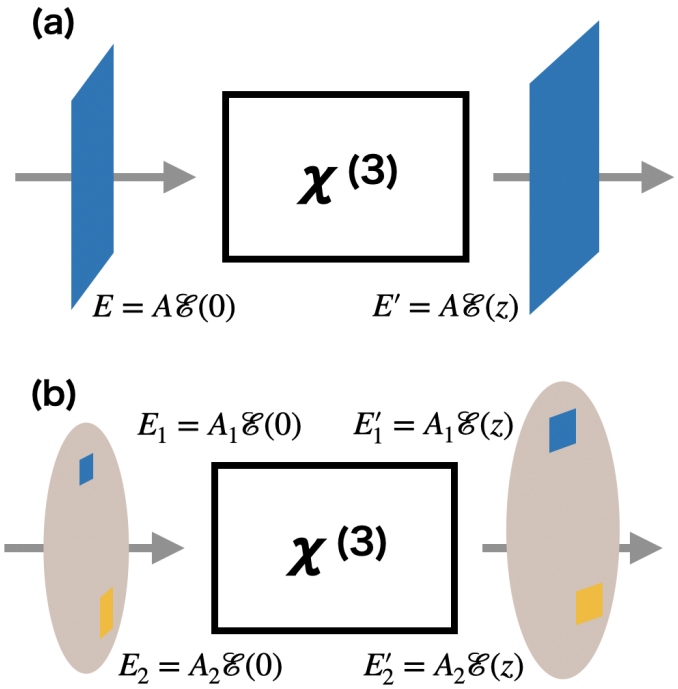

Figure 6.1: (a)When the input field is plane wave, Eq. 6.6 can be solved analytically, the amplitude of the wave will change but its perpendicular profile remains the same. (b) When input becomes LG mode beams, we assume each component will be amplified on their own, ignoring interaction between different components in the beam.

However, for LG mode beams, the complicated perpendicular profile will hugely increase the computation difficulty. Therefore we will make another simplification here, ignoring the second term on the left hand side as if our input beam is composed of many infinitesimal plane wave. During the FWM process, each of the infinitesimal component will be amplified differently since they have different amplitude to begin

with. This situation is shown in Fig. 6.1(b). We should be aware that this simplification completely ignores the interaction between different components of the beam (this is the physical interpretation of the second term on the lefthand side.) However this effect is small in our setup since our cell is short and the beam components will leave the cell before they can interact too much.

In the end, our Mathematica program numerically solves the following coupled first-order differential equations.

$$\frac{\partial}{\partial z}\mathcal{E}_{Stokes} = \frac{ik_{Stokes}}{2\epsilon_0}[3\chi_{1221}\mathcal{E}^2_{pump}\mathcal{E}^*_{probe}] \tag{6.7}$$

$$\frac{\partial}{\partial z}\mathcal{E}_{probe} = \frac{ik_{Stokes}}{2\epsilon_0}[3\chi_{1221}\mathcal{E}^2_{pump}\mathcal{E}^*_{Stokes}] \tag{6.8}$$

In our toy system, the wave vector k is the same for probe and Stokes. We can thus set the coefficient $ik/2\epsilon_0 = 1$,assuming perfect phase matching To solve this set of equations, we need the initial condition for Stokes and probe field. In our setup, since there is no Stokes field before FWM, Stokes field is set to zero. Probe field, on the other hand, takes the value of whichever LG mode we set it as.

6.3 Stokes and probe profile

In this section, we will briefly show the sample Stokes and probe profile when we set the beam parameters to our experiment setup. $r_{pump} = 300\mu m$, $r_{probe} = 130\mu m$. In this example, we set the pump to LG(0,0) mode, and the probe to a superposition of (3,2) and (-3,2) mode. The intensity and phase profile of input fields are shown in Fig. 6.2. In the probe intensity profile we see the familiar petal pattern as we see in the experiment, and the ring structure that should present with $p \neq 0$ modes. In the probe phase profile we see that the phase varies in different position, agreeing with

the theory picture in Eq. 2.12

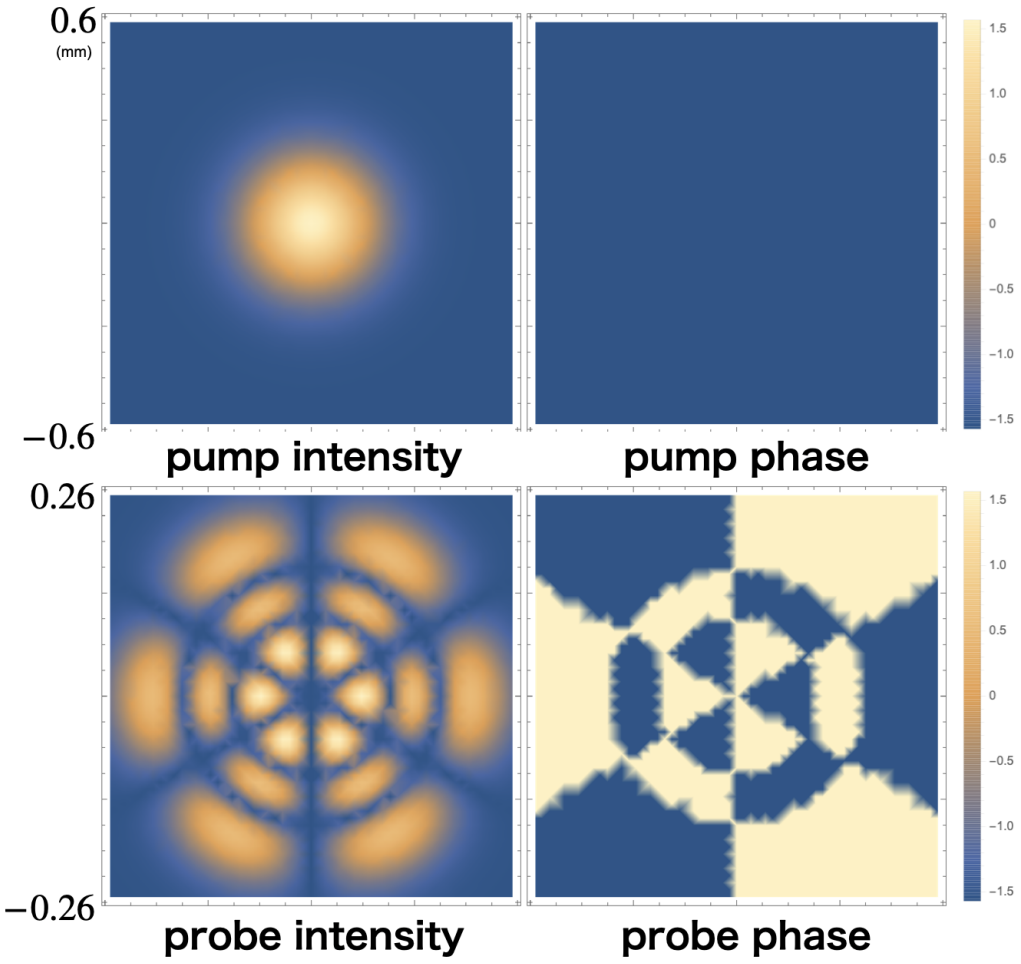

Figure 6.2: Sample intensity and phase profile of pump and probe when we set the parameters the same as our experiment. Note that the two figure are not on the same scale.

We then input the fields into the coupled differential equation and monitor the output of the Stokes intensity and phase profile. Our program should obey the OAM conservation rule stated in Eq. 2.22, sharing the same dominant mode with probe with the opposite sign. In our case, since the probe is (3,2)+(-3,2) mode, therefore Stokes should be (-3,2)+(3,2) mode, which is the same as input. Moreover, phase of the Stokes beam should be conjugated to the phase of probe beam as a consequence

of FWM. Our simulation result is shown in Fig. 6.3.

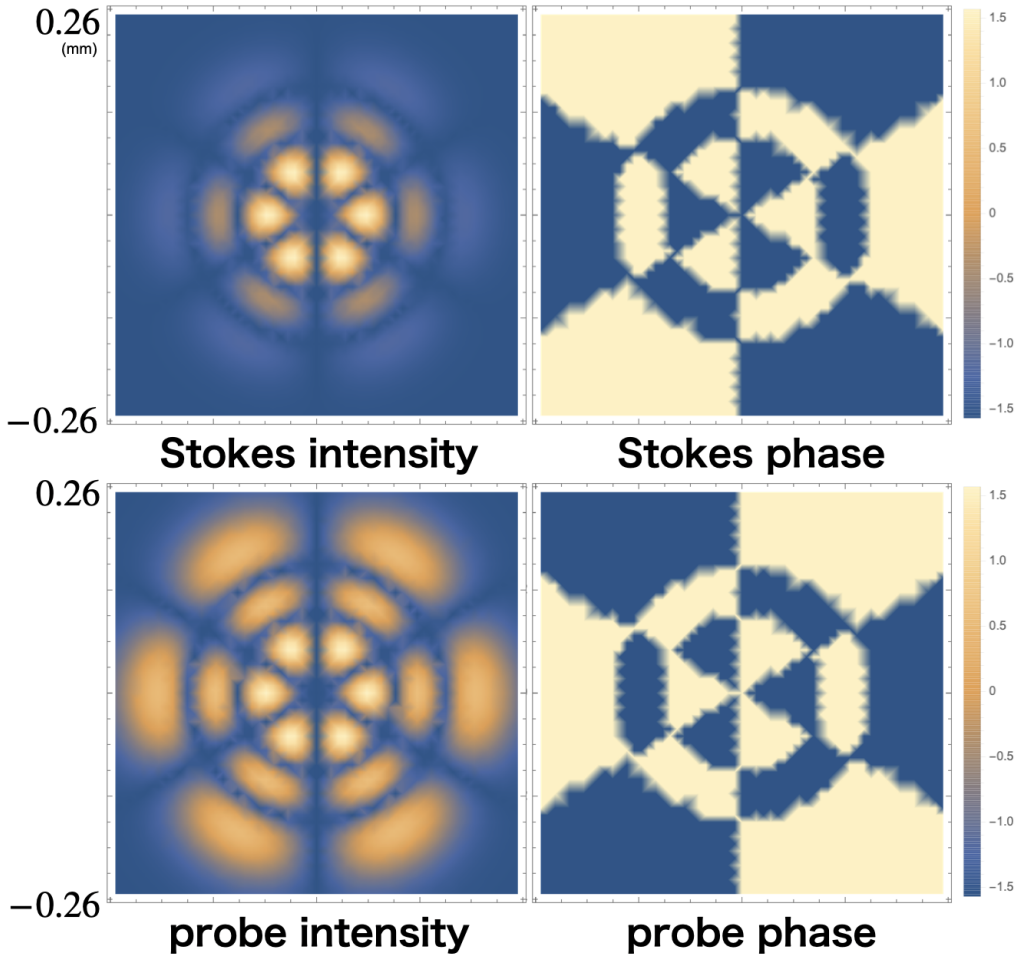

Figure 6.3: Sample intensity and phase profile of probe and Stokes when we set the parameters the same as our experiment. The Stokes has the same dominant mode and conserves OAM. However, its intensity on the outer ring is much lower comparing to the probe.

Just by looking at the intensity profile of Stokes, we can already tell that it is not 100% the same as the input probe, meaning that there must be other modes presenting in the Stokes beam besides the dominant (3,2)+(-3,2) mode. However, it looks like l mode is conserved, (the phase map of Stokes is the same as in Fig. 6.2), it is p index that is a problem. In the following sections, we will investigate the

relationship between the size of the input beams and the mode decomposition of Stokes mode that we get.

6.4 FWM efficiency under different probe size

The first calculation that we do is to look at the intensity of Stokes beam with respect to different probe beam size. In our experimental setup, the total probe power is fixed. However, probe beam size can be adjusted through combination of lens. The focusing of beam can bring two effects. On one hand, the intensity in the center region of probe field will be higher, however on the other hand the wave vector $\vec{k}$ of the incoming probe field will have a wider spread of direction and will result in phase mismatch $\Delta\vec{k}$ as described in Eq. 2.9. In reality we want to find a balance between these two effects. However since in our program focusing effect is not considered, we will model the beam as collimating beams with various radii. This will not give us the most precise result, but will still qualitatively tell us whether FWM efficiency is sensitive to beam radius. In experiment we can use a telescope to change the size of a collimated beam. It is just more work.

In order to simulate the effect of a lens, we need to renormalize our probe beam so that beam of different radius still share the same power. We control the power to be $162\mu W$, which is the power that we get when we run the program in parameters that agree with our experiment. I want to point out here that the absolute value of power in our simulation is not meaningful, as we have set multiple physical constants to 1. Our result cannot be directly comparable to the experimental result, but should follow similar trend. The renormalized intensity profile of 3 different probe beam: $w_0 = 130\mu m$, $w_0 = 65\mu m$, and $w_0 = 32.5\mu m$ in LG mode (2,0) is shown in Fig. 6.4.

We couple these three probe beams to a Gaussian pump beam of $w_0 = 300\mu m$, which is the same as our experiment. The resulting Stokes beam intensity profile is

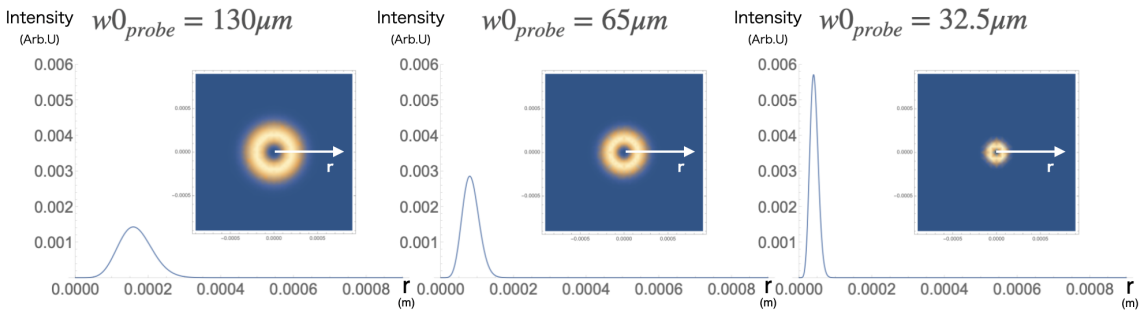

Figure 6.4: Intensity profile for input probe beam of three different sizes. All of their power is renormalized to 162μW. Smaller beam has a higher amplitude near origin but a narrower spread, while larger beam has a lower intensity but a wider spread over radius.

shown in Fig. 6.5.

We notice that the shape of each intensity profile resembles the shape of their corresponding input. However, the configuration on the left (largest probe) has a much weaker coupling than the rest two configurations. When we decrease the radius of beam from the original 130μm to half its value, the coupling efficiency doubles. However when we further decrease the beam radius by half, the Stokes power only increased slightly, for about 25%. Therefore we can conclude that the original beam radius setting is not optimal, and we should focus the beam more tightly. The effect of shrinking beam size will be smaller and in experiment we should be able to find a turning point where the increase of power due to focusing become smaller comparing to the decrease of power due to phase mismatch, and that is where we should stop.

6.5 p mode information preservation

In Chapter 5, we experimentally confirmed OAM conservation in degenerate FWM process. We concluded that although we see more noise in beam with higher l mode, the information contained in l mode is fairly well preserved. In this section we will

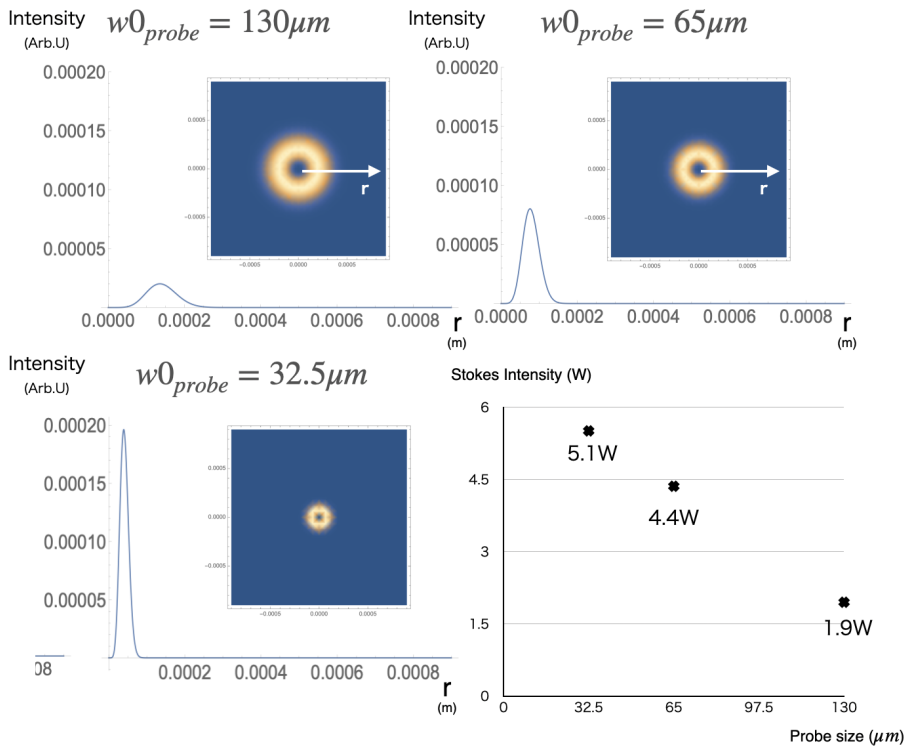

Figure 6.5: Intensity profile for output Stokes beam of three different sizes. In general, smaller probe size generates smaller but higher power Stokes beam. Notice that the FWM efficiency in the original setting (left) is much worse comparing to the other two.

look at the radial mode, p mode, and check whether if p mode information is also preserved in degenerate FWM.

Fig. 6.6 shows the Stokes beam along with its intensity profile when we set beam size equal to experiment ($w_{pump} = 300\mu m$,$w_{probe} = 130\mu m$), with pump in (0,0) and probe in (3,3) mode. When we compare the Stokes beam profile in the middle with the probe input on the left, we can tell that the radial structure, especially that of outer rings are not very well preserved in this configuration as the intensity drops dramatically.

To quantatively analyze the mode composition in the Stokes beam, we have to rely

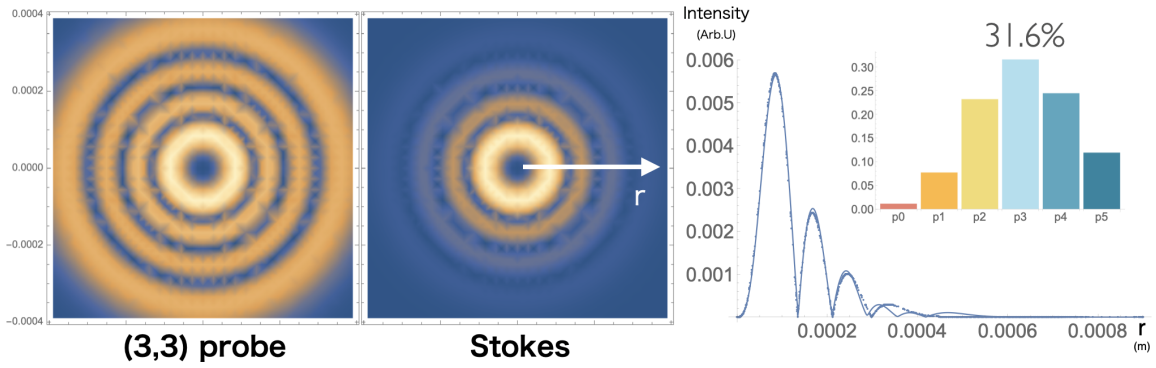

Figure 6.6: Intensity profile of Stokes beam when $w_{pump} = 300\mu m$,$w_{probe} = 130\mu m$, pump=(0,0), probe=(3,3) The outer ring intensity of Stokes is much weaker comparing to the pure (3,3) mode probe beam. The dominant p=3 is only 31.6% in mode decomposition.

on mode decomposition. The advantage of using simulation instead of experimental image is that the generated Stokes is perfectly spherically symmetric. Therefore we chose to fit only the intensity profile on $\theta = 0$ axis. However in this case, we need to limit the mode which our program fit onto. Since through the Mach-Zehnder interferometer introduced in Chapter 5, we can obtain reliably good l mode information already, we decided to set the l mode to the dominant mode. (In this particular case, $l = 3$) We then fit the Stokes intensity profile shown on the right side of Fig. 6.6 to $l = 3$, $p = 0 - 5$ mode. The best fit suggests that the dominant $p = 3$ mode only constitute 31.6% of the Stokes beam. If we examine the best fit closer, we can see that in the fit also has some tiny discrepancy with the intensity profile, suggesting that there are even higher p mode components. However in order to control the degree of freedom and avoid the problem of overfitting, we ignored higher p modes and constrained our analysis upto $p = 5$.

Next we repeated the same process for different probe input sharing $l = 3$ but different p number from 0 to 3. The intensity profile and p mode decomposition results are shown in Fig. 6.7. We can see that with the increase of p number, the

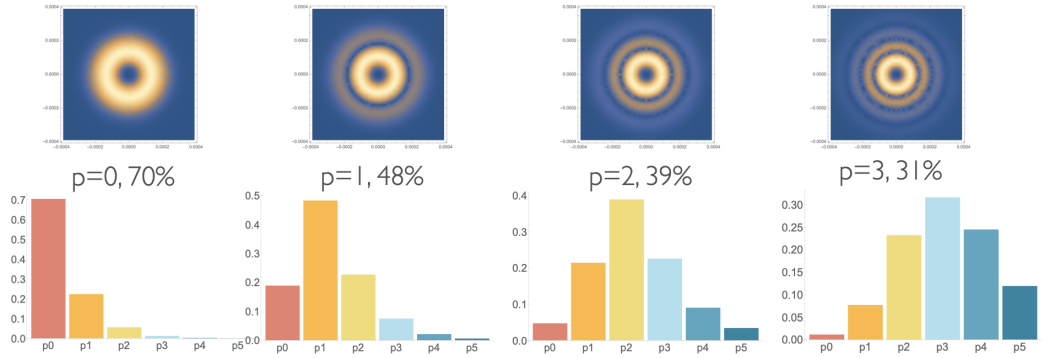

Figure 6.7: Intensity profile and mode decomposition results for different probe input beam with $l = 3$, $p = 0 - 3$. In each case, the dominant mode and its percentage is shown under the beam profile. The dominant mode component decrease as the p number increase, but generally all of them are noisy.

dominant p mode component decreases. In general p mode information is not very well preserved. Even in $p = 0$, where the dominant mode component is the highest under this beam configuration, there is still only 70% of dominant mode where the rest 30% consists of higher p modes. This can be concerning if we try to transmit information through p mode since most of the information will be lost on its way.

To increase the p mode information preservation, we try to change our beam size. For this purpose we can change either the pump size or the probe size. For simplicity, we chose to change the pump size this time. We first tried to shrink the pump size to the limit that the pump size equals that of probe. $w_{pump} = w_{probe} = 130\mu m$. Fig. 6.8 shows the intensity profile and mode decomposition results when we input (3,0) and (3,2) mode probe and (0,0) mode pump.

From Fig. 6.8, we see that as the pump size shrinks down, the dominant mode becomes even less dominant, even totally covered up by other "noise" modes. This makes sense as a smaller pump size will decrease the coupling between pump and probe, especially in the outer region. This is also shown in the intensity profile of the Stokes beam generated. Especially in the $p = 2$ case, as we can tell from Fig. 6.8, the

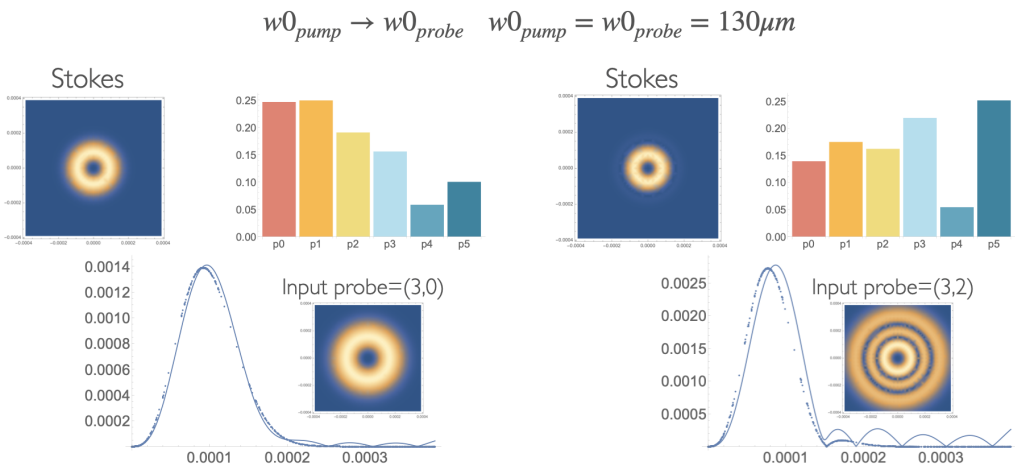

Figure 6.8: Intensity profile and mode decomposition results for (3,0) and (3,2) probe input when $w_{pump} = w_{probe} = 130\mu m$. The fit fails to give a good fit result, and the dominant mode is totally covered up by other modes. From the intensity profile, we can se that the ring structure is not preserved at all, and thus information is greatly damaged.

outer ring structure is completely lost. The best fit the program gave also fail to fit the intensity profile properly, providing multiple "ripples" at the end of the fit. This is another evidence of even higher mode present in the Stokes output.

If shrinking pump size decrease the p mode information preservation, then we should predict that increasing the size of pump will increase the dominant p mode component in the Stokes beam. This is also simulated with our program, under the same condition of probe in (3,2) mode, but different size of pump.

By looking at Fig. 6.9, we can qualitatively conclude that with the increase in pump size, the coupling between pump and probe becomes better, and thus the Stokes are more amplified in the outer region. In fact, if we compare the pure (3,2) mode probe, which is circled in the yellow rectangle, with the $w_{pump} = 8w_{probe}$ case, the two beam almost look identical, and we really need the assistance of p mode decomposition to tell the noises in this case.

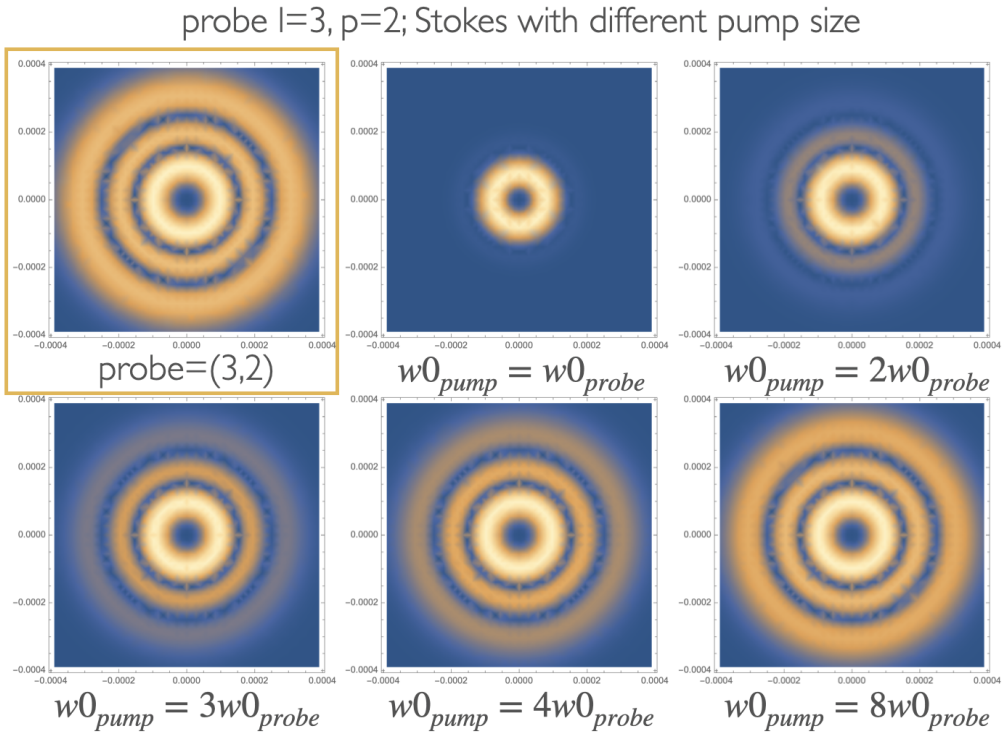

Figure 6.9: Intensity profile of Stokes beam with different pump size but the same probe in pure (3,2) mode. The probe image is in the upper left corner, circled in the yellow rectangle. We simulated 8 data points, with $w_{pump} = 1/2/3/4/8w_{probe}$. As the pump size increase, the outer ring structure becomes more clear, and p mode information is better preserved.

The mode decomposition result for $w_{pump} = 8w_{probe}$ is shown in Fig. 6.10(a). This time the dominant mode increases to 89%, which is much larger than 39% as in the simulation result for our current experimental setup. In Fig. 6.10(b), we have shown the trend of dominant mode for (3,2) mode probe when we increase the pump size. We can see that as we increase the pump size, the dominant mode component also increases, confirming our prediction.

Lastly, we tested the same trend for not only $p = 2$ modes, but other p modes as well. Fig. 6.11 shows the trend of dominant mode for different p modes when we increase the pump size. We can conclude that it is a general trend that when the

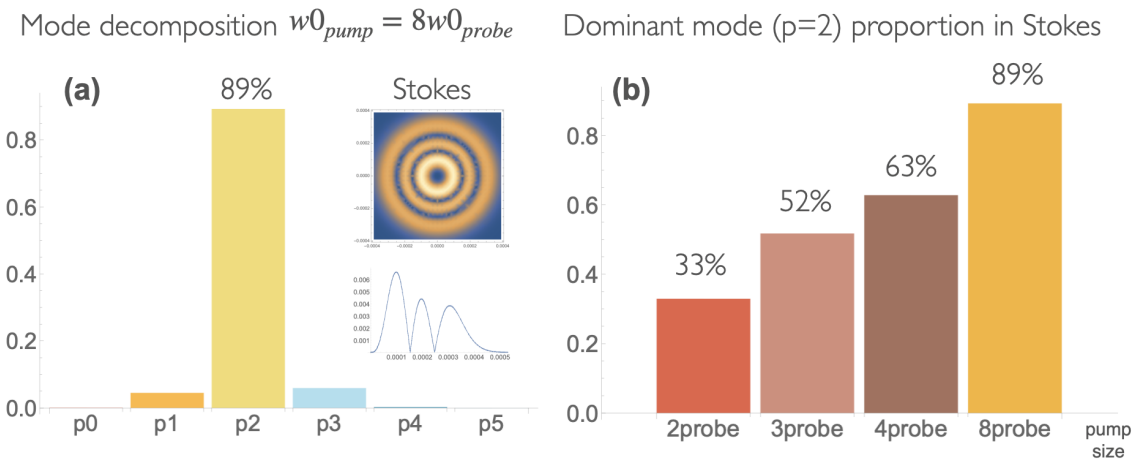

Figure 6.10: (a) Mode decomposition result for $w_{pump} = 8w_{probe}$, the dominant mode ($p = 2$) reaches 89%, the noise is very small comparing to the dominant mode. (b) The dominant mode component plotted against different pump size. The larger the pump, the higher the dominant mode component becomes.

pump is larger, (thus when the probe interact with higher power region of the pump), the p mode information is better transmitted through FWM. When $w_{pump} = 8w_{probe}$, dominant mode in the system all reaches above 80% and can be considered a good preservation. We think this number will keep increasing if we increase the beam size even further.

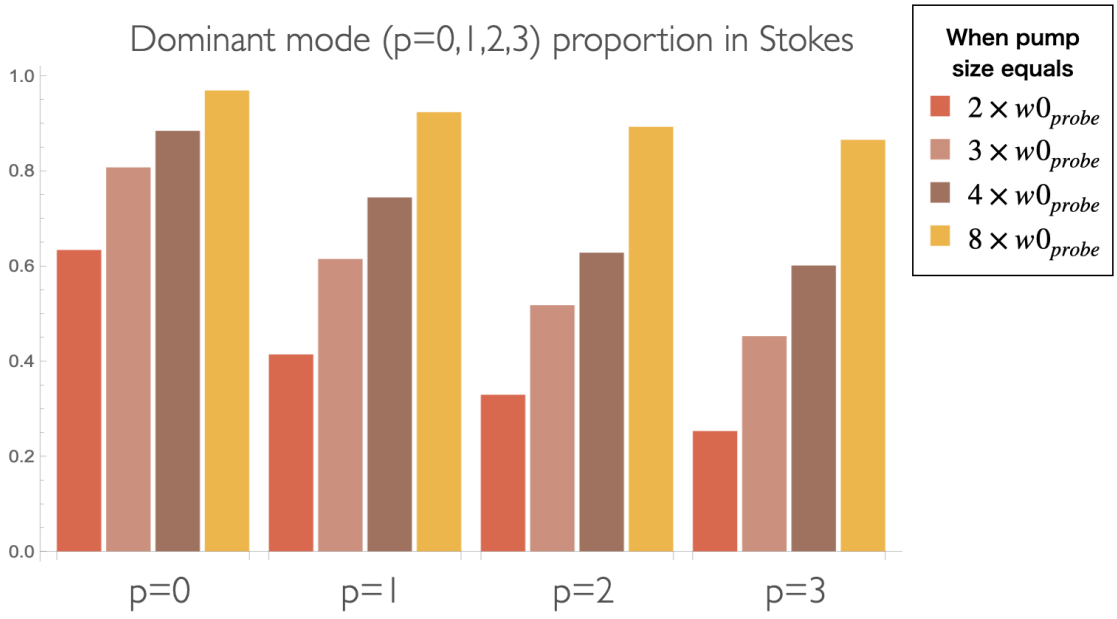

Figure 6.11: The dominant mode percentage with respect to various pump radii. For each p number, as the pump size increase, the dominant mode component also increases. This effect is especially large for higher p numbers like in $p = 2$ or 3

Chapter 7

Conclusions and Next Steps

7.1 Conclusion

In our experiment, we successfully established an experimental platform which realized degenerate FWM with two co-propagating, orthogonally polarized beam. We experimentally confirmed that our experimental scheme conserve OAM fairly well up to $l = 8$, although higher l modes do contain more noise.

We also built a sample FWM model which can reproduce the most basic function of our experimental apparatus, and qualitatively confirmed that under the same total probe power, smaller probe size gives us better FWM efficiency. Moreover, we also found that p mode information is not well preserved in our current experiment configuration. Increasing the pump beam size will improve the transmission of p mode information.

7.2 Next Steps

Looking ahead, we think there are several directions that will be interesting and helpful to explore in order to improve our result. Firstly, we would like to compare our simulation to experimental data, especially that of probe focus. While the simulation result suggests that smaller probe gives higher FWM efficiency, in reality we have

to keep track of the influence due to phase match. We are interested in finding a good balance point between these two effects both experimentally and theoretically. Several experimental trials have actually been made to implement focusing lens into the system, but due to physical restriction of our experimental setup, we did not find a reliable way of measuring Stokes power with focusing lens. It would be very ideal if we could find a way to measure the Stokes power with different focusing probe, as well as finding a way to model this effect into our theoretical model, which needs more complication than it currently has.

Another direction that is interesting to investigate would be adding a separate source other than the laser that we use for pump and probe as a repump. The repump will couple with the original pump and probe. According to rules of phase conjugation, it will be able to provide a backward Stokes beam that has the potential to increase FWM gain even further.

Appendix A

Public Abstract

Here I attach the public abstract that is required for this thesis to meet the requirement for COLL400 curriculum.

Introduction and Background

Efficient ways of communication becomes crucial in our everyday life due to the increase in the demand of large-size information exchange. As we step towards the next generation of quantum communication, it is important to explore the possibility of new potential modes for communication that can compliment the current standard: amplitude modulation and frequency modulation. One of the candidates that have potential for increasing the data line capacity of high-quality communication is the transverse spacial mode of light, in other words, the cross-section shape of the light beam when it is traveling in space. The aim of my project thus is to investigate, and further control the quality of the shape of laser beam during propagation through nonlinear and quantum optical processes, as well as studying reliable ways of extracting information from this mode. More particularly, I focus on the generation and decomposition of light beams carrying Orbital Angular Momentum (OAM) via degenerate four-wave mixing (FWM) in Rubidium vapor.

Summary of Result

We used light in different combinations of Laguerre-Gaussian (LG) modes as input

source and looked at how the output mode after FWM process varies from the input. From our experiment, we found that FWM preserves most of the angular information but does not preserve radial information.

Intellectual Merit

The intellectual merit of my project is to develop an experimental platform which integrates all the basic steps of telecommunication, from generation to mode decomposition of light with different transverse spacial mode. Moreover, my system is different from previous experiments in two ways. Firstly, my experiment generates not one, but two, quantum entangled beams carrying conjugated modes. The correlation between the pair of twin beams will help to suppress the noise and increase the quality of signal. Secondly, the twin beams co-propagate, and share the same frequency. This is unique compare to previous setups, in which the two beams had different frequencies, and can expand the span of application to a broader range of situations, where a single frequency source is preferred.

Broader Impact

In a broad sense, the goal of my project is to help developing a sufficient way of high-data-rate transmission that will be applied in the near future. The success in multi-spacial-mode beam transmission can change the way communication standards are set, and can boost both the speed and security of information communication to a new level. The technology itself is vital to national security and globalization. But more importantly, the understanding of nonlinear and quantum optical processes will serve as the bridge between our classical world and quantum phenomena that completely change the way we perceive the world.

Bibliography

[1] L. Allen, M.W. Beijersbergen, R.J.C. Spreeuw, and J.P. Woerdman. Orbital angular momentum of light and the transformation of laguerre-gaussian laser modes. *Physical Review. A*, 45(11):8185–8189, June 1992.

[2] G. Gibson and et al. Free-space information transfer using light beams carrying orbital angular momentum. *Optics express*, 12(22):5448–56, Nov 2004.

[3] G Xie and et al. Experimental demonstration of a 200-gbit/s free-space optical link by multiplexing laguerre-gaussian beams with different radial indices. *Optics Letters*, 41(15):3447–50, Aug 2016.

[4] A. Mair, A. Vaziri, G. Welhs, and A. Zeilinger. Entanglement of the orbital angular momentum states of photons. *Nature*, 412, July 2001.

[5] R.F. Offer, D. Stulga, E. Riis, S. Franke-Arnold, and A.S. Arnold. Spiral bandwidth of four-wave mixing in rb vapour. *Communications Physics*, 1(1):1–8, Nov 2018.

[6] R.W. Boyd. *Nonlinear Optics*. Academic Press, 2003.

[7] N. González, G. Molina-Terriza, and J.P. Torres. How a dove prism transforms the orbital angular momentum of a light beam. *Optical Express*, 14(20):9093–9102, 2006.

[8] N. Super and I. Novikova. Two-mode squeezing and conservation of optical angular momentum via four-wave mixing in rubidium, 2018.

[9] R. Ma and et al. Generating quantum correlated twin beams by four-wave mixing in hot cesium vapor. *Phys. Rev. A*, 96(4), 2017.

[10] A.M. Yao and M.J. Padgett. Orbital angular momentum: origins, behavior and applications. *Adv. Opt. Photonics*, 3(2):161–204, 2011.

[11] R.N. Lanning and et al. Gaussian beam-propagation theory for nonlinear optics - featuring an exact treatment of orbital angular momentum transfer. *Phys. Rev. A*, 96(1), 2017.

[12] A. Yariv and P. Yeh. *Optical waves in crystals : propagation and control of laser radiation*. New York : Wiley, 1984.

[13] D.L. Mills. *Nonlinear Optics: Basic Concepts*. New York: Springer, 2nd edition, 1998.

[14] M.J. Padgett. Orbital angular momentum 25 years on. *Optical Express*, 25(10):11265–11274, May 2017.